

Improving the reliability of photometric redshift with machine learning

Oleksandra Razim^{1*}, Stefano Cavuoti^{2,1}, Massimo Brescia²,
Giuseppe Riccio², Mara Salvato³, Giuseppe Longo¹

¹Department of Physics, University Federico II, Strada Vicinale Cupa Cintia, 21, 80126 Napoli, Italy

²INAF - Astronomical Observatory of Capodimonte, Salita Moiariello 16, I-80131 Napoli, Italy

³MPI for Extraterrestrial Physics, Giessenbachstrasse 1, Garching b. München, 85748, Germany

Accepted XXX. Received YYY; in original form ZZZ

ABSTRACT

In order to answer the open questions of modern cosmology and galaxy evolution theory, robust algorithms for calculating photometric redshifts (photo- z) for very large samples of galaxies are needed. Correct estimation of the various photo- z algorithms' performance requires attention to both the performance metrics and the data used for the estimation. In this work, we use the supervised machine learning algorithm MLPQNA to calculate photometric redshifts for the galaxies in the COSMOS2015 catalogue and the unsupervised Self-Organizing Maps (SOM) to determine the reliability of the resulting estimates. We find that for $z_{\text{spec}} < 1.2$, MLPQNA photo- z predictions are on the same level of quality as SED fitting photo- z . We show that the SOM successfully detects unreliable z_{spec} that cause biases in the estimation of the photo- z algorithms' performance. Additionally, we use SOM to select the objects with reliable photo- z predictions. Our cleaning procedures allow to extract the subset of objects for which the quality of the final photo- z catalogs is improved by a factor of two, compared to the overall statistics.

Key words: methods: data analysis – techniques: spectroscopic – catalogue – surveys – galaxies: distances and redshifts

1 INTRODUCTION

Knowledge of spatial distribution of galaxies is crucial for answering most of the open questions in observational cosmology and galaxy evolution. In particular, we need to know galaxy distances. The universal method of deriving them is to measure redshifts of galaxies, caused by the cosmological expansion. The most accurate way of doing that is to calculate spectroscopic redshifts (spec- z , or z_{spec}), but this method requires high-quality spectra for all investigated objects. Obtaining these spectra is time-consuming and sometimes impossible for the faint sources. Currently, wide-field galaxy surveys cannot provide spec- z catalogues of the same depth and richness as photometric catalogues. For example, for the 16-th Data Release of the Sloan Digital Sky Survey (SDSS) the ratio between the number of detected galaxies and the number of available spectroscopic redshifts is of the order of $1/100^1$, going down to even smaller numbers for other surveys.

This difficulty of deriving galaxy redshifts from spectra led to the development of alternative techniques, collectively called *photometric redshift methods* (photo- z , or z_{phot}), first proposed in Baum

1957, 1962 and further investigated in a vast number of publications, e.g. Baldwin 1977, Butchins 1981, Koo 1985, Connolly et al. 1995, Gwyn & Hartwick 1996, Bolzonella et al. 2000, Benítez 2000, Collier & Lahav 2004, Ball et al. 2008, Brammer et al. 2008, Gerdes et al. 2010, Carrasco Kind & Brunner 2013, 2014, Hoyle 2016, Bonnett et al. 2016, Sadeh et al. 2016, Bilicki et al. 2018, Pasquet et al. 2019 and many others.

These methods are based on the fact that multi-band photometry can be treated as a low-resolution spectrum and hence as an approximation of the intrinsic Spectral Energy Distribution (SED). Cosmological redshift causes a stretching of the SED and a change in the wavelengths of the prominent spectral features (Lyman or Balmer breaks, emission and absorption lines, etc.) that, moving in or out of the fixed bands of a given photometric system, cause changes in magnitudes and colours. From these changes we can derive photo- z .

There is a variety of photo- z estimation methods. The majority of them uses one of the two main approaches: a theoretical one, called SED template fitting, and an empirical one, largely based on machine learning (ML) paradigms (Euclid Collaboration et al. 2020, Schmidt et al. 2020).

SED template fitting methods use spectral template libraries obtained from either observations or galaxy models. These templates are shifted across the expected redshift range (using an ar-

* E-mail: shr.razim@gmail.com

¹ Based on the sizes of photometric and spectroscopic catalogues obtained via <http://skyserver.sdss.org/CasJobs/>

bitrarily chosen step) and then convoluted with the transmission curves of the acquisition system in order to derive estimated magnitudes. The resulting magnitudes are then fitted to the observed data in order to find the combination of a template and redshift value which minimise the residuals. Depending on the particular approach, template fitting methods may include such steps as producing new templates via interpolation between the already existing ones, correcting systematic biases of the observed photometry, compensating for the absorption of the interstellar medium, etc. A downside of these methods is that they require template libraries that are conditioned by our knowledge of galaxy evolution and therefore by definition incomplete.

Instead of using pre-defined templates, ML derives the correlation between photometry and redshift from the data themselves. To train the ML models we need a knowledge base (KB), formed by both photometry and high-quality spec-z for a considerable number of objects (how large depends on the homogeneity of the sample under scrutiny). With a KB large enough and fully covering the parameter space, the ML approach allows to take into account all observational and physical effects automatically (Brescia et al. 2018). At the same time, providing a high-quality KB is not a trivial task by itself. For instance, due to the fact that ML methods have a limited extrapolating power, they cannot provide reliable photo-z predictions outside the spectroscopic range covered by the KB. This is particularly relevant in the faint object domain, usually not properly covered by spectroscopic surveys.

To provide best performance, SED fitting and ML require different types of data, and for this reason the areas of application of the two methods are slightly different (Salvato et al. 2019). In the low-redshift regime ML photo-z often perform better than SED fitting methods, provided that a well-representative spectroscopic KB exists. For high-redshift objects, SED template fitting usually shows better results, mostly due to the lack of a consistent KB for these galaxies. Furthermore, in the case of severe depth imbalance between spectroscopic and photometric information, SED fitting can be the only option.

Lately, hybrid photo-z techniques that unite strengths of both approaches have appeared (see e.g. Newman 2008, Beck et al. 2016, Cavuoti et al. 2017b, Duncan et al. 2018). Still, at this point no method allows to estimate photo-z with the same precision as high quality spec-z. Currently, the accuracy of spectroscopic redshift surveys can reach an error of $\sigma \sim 10^{-3}$, where σ is a standard deviation of the distribution of residuals between repeated measurements of spec-z of the same objects (e.g. Le Fèvre et al. 2005, Hasinger et al. 2018). The accuracy of photo-z catalogues obtained with broadband photometry is characterized by $\sigma \sim 0.02$ at best (Laureijs et al. 2011, LSST Science Collaboration et al. 2009, Salvato et al. 2019, Brescia et al. 2014), where σ describes the distribution of residuals between spec-z and photo-z. Nevertheless, for the upcoming massive surveys, such as the Rubin Observatory Legacy Survey of Space and Time (LSST, Ivezić et al. 2019) and the Euclid (Laureijs et al. 2011), deriving photo-z is the only realistic way to obtain distances for the majority of the observed galaxies, so further improvements of photo-z methods are required.

Among the many factors that affect the quality of the photo-z are the issues related to the completeness and quality of the spectroscopic catalogues used for SED fitting calibration and ML training. Firstly, incompleteness of spec-z sample limits the performance of photo-z algorithms, especially the ML ones. Usually spec-z catalogues are incomplete in the faint part of the magnitude parameter space, but the selection function of the spec-z observations may affect the performance in the whole range of magnitudes. Second,

the miscalculated spec-z affect the reliability of the performance metrics used for the estimation of quality of photo-z. Some percentage of miscalculated or misidentified sources is present even in the spec-z samples that are believed to be reliable. Typical high-confidence redshift quality flags provide us with 95-99% of reliable sources, implying that 1-5% of sources have unreliable spec-z. Consequently, there is no way to say which of the photo-z outliers are due to miscalculated photo-z and which are related to incorrect spec-z values.

For small-size surveys the objects with noticeable difference between spec-z and photo-z can be manually inspected (see e.g. Lanzetta et al. 1998 and Masters et al. 2017), but for large-scale surveys this is not feasible. As a result, we have to find a way of disentangling the various contributions to the error budget, i.e. to distinguish the photo-z prediction error induced by the defects of an estimation method from the uncertainty carried by the contamination of the spectroscopic data.

In this work we present a data cleaning methodology, focused on handling these two data-related issues, namely:

- identifying unreliable spec-z;
- deriving from the photometric catalogue a set of objects that can be considered as well-represented by the spec-z catalogue, and therefore trusted in terms of photo-z quality estimations.

As we will show, both procedures allow to significantly improve the quality of the final photo-z catalogues.

Our methodology is based on the Self-Organizing Map (SOM) algorithm, first proposed in Kohonen (1982), and on an approach proposed in Masters et al. (2015, 2017). For the photo-z calculation we use 30-band photometric data from the COSMOS2015 catalogue (Laigle et al. 2016), the master spec-z catalogue provided by COSMOS collaboration (obtained via private communication with Mara Salvato), and the Deep Imaging Multi-Object Spectrograph (DEIMOS) spec-z catalogue (Hasinger et al. 2018). To obtain photo-z we apply the Multi Layer Perceptron with Quasi Newton Algorithm (MLPQNA, Brescia et al. 2013, 2014). For additional testing of our data cleaning methodology we also use the SED template fitting photo-z catalogue described in Laigle et al. (2016).

This paper is organized as follows. Section 2 explains how we obtain and pre-process our data. In Section 3 we describe our algorithms, and in Section 4 we describe the experiments on calculating the photo-z and improving their quality with the SOM. Section 5 contains the discussion of the results. The conclusions are stated in section 6. The Jupyter notebooks necessary to reproduce the work are available for download via GitHub repository https://github.com/ShrRa/COSMOS_SOM. MLPQNA is available as a part of PhotoRAPTOR software (Cavuoti et al. 2015a). The final photo-z catalogue will be published via CDS Vizier facility.

2 DATA

In this section we describe the three catalogues used in this work:

1. COSMOS2015, which is our source of photometric measurements and SED fitting photo-z. Its detailed description can be found in Laigle et al. (2016).
2. A compilation of spectroscopic redshifts available in literature for the same COSMOS field. We will call this catalog our main spec-z catalog.
3. The Deep Imaging Multi-Object Spectrograph (DEIMOS)

spec-z catalogue (Hasinger et al. 2018), used to perform an additional, independent test of our methods. Same as the main spec-z catalogue, the DEIMOS sample covers most of the COSMOS2015 field.

2.1 COSMOS2015 photometric catalogue

The COSMOS2015 catalogue contains multi-wavelength broad-range (from mid-IR to near-UV) photometry for about half million objects, for which X-Ray and radio measurements, star formation rates and other additional information is available. Moreover, this catalogue includes SED fitting photo-zs, obtained with LePHARE software (Arnouts et al. 1999, Ilbert et al. 2006).

One of the most important aspects to consider in any ML based experiment is the selection of the training parameter space, i.e. input features that maximize the amount of suitable information. In the case of ML methods for photo-z this problem has been widely discussed (cf. D’Isanto et al. 2018, Brescia et al. 2018, and references therein). From the ML point of view, an automatic feature selection is not a trivial task: many algorithms for feature selection exist and have been tested on the problem (see Donalek et al. 2013, Baron 2019, Brescia et al. 2019), as well as some data driven brute force approaches (Polsterer et al. 2014, D’Isanto et al. 2018), which may provide optimal results at the price of very high computational costs, making it impossible to use it on massive and high-dimensional datasets.

In this work, we do not perform an all encompassing feature selection investigation. Instead, we try several feature sets, based on general physical considerations and our past experience. To try these different feature sets, we downloaded the COSMOS2015 photometric data consisting of 34 bands:

- UV broad and medium bands: NUVmag, FUVmag, u;
- optical and near-IR broad bands: B, V, ip, r, zp, zpp, Ks, Y, H, J, Hw, Ksw, yH;
- mid-IR broad bands: 3_6mag, 4_5mag, 5_8mag, 8_0mag;
- optical and near-IR medium bands: IA484, IA527, IA624, IA679, IA738, IA767, IB427, IB464, IB505, IB574, IB709, IB827;
- and optical and near-IR narrow bands: NB711, NB816.

For all of them 2'' and 3'' apertures were available, except for Spitzer Large Area Survey with Hyper-Suprime-Cam (SPLASH; 3_6mag, 4_5mag, 5_8mag, 8_0mag) and GALEX (NUVmag, FUVmag) bands.

The pre-processing of this dataset consisted of the following steps:

1. To ensure homogeneity of photometry and to enable a comparison with SED fitting photo-z, we follow the procedure described in Laigle et al. 2016. We consider only those objects that lay within both UltraVISTA (this is done by using the condition `Area==0`) and COSMOS (`Cf1==1`) sky areas (see McCracken et al. 2012, Capak et al. 2007 and Scoville et al. 2007 for a detailed descriptions of these regions). As a result we extract 576,762 objects out of the initial 1,182,108 samples available.
2. We also exclude stars, X-ray and unclassified sources (`OType==0`). This leaves us with 551,538 objects.
3. Finally, we remove saturated sources, by rejecting objects masked in optical broad bands (`Sat==0`). After this step, the final photometric catalogue consists of 518,404 objects.

2.2 Main Spectroscopic catalogue

The main spec-z catalog is extracted from the spectroscopic COSMOS master catalog maintained within the COSMOS collaboration and it includes only the publicly available redshifts prior Fall 2017. This catalogue contains 65,426 spectral redshifts, obtained with 27 different instruments in a spec-z range $0 < z_{\text{spec}} < 6.5$. The pre-processing consisted of the following steps:

1. To exclude stars, we remove sources with $z_{\text{spec}} < 0.01$; we also remove objects with $z_{\text{spec}} > 9$ to discard likely erroneous spec-z;
2. AGNs often pose a contamination problem for photo-z algorithms (Norris et al. 2019). Therefore, we remove sources visible in X-Ray, using a catalogue of AGN sources detected by Chandra in the COSMOS field (Civano et al. 2012).
3. Then we clean the resulting spec-z catalogue from unreliable instances, using the available quality flags `Q_f`, described in Lilly et al. (2009). We select only robust spectroscopic redshifts (i.e. with $\sim 99.6\%$ of spectroscopic verification), using the conditions $2 < Q_f < 5$ and $22 < Q_f < 25$.

It is important to note that the Main spec-z catalogue is a compilation of multiple catalogues. These data were obtained during different surveys with different targeting strategies and quality requirements during the last two decades, so the exact quality of the spectroscopic verification is impossible to estimate. As a result, the actual robustness of the final spec-z set may be lower, and this is one of the issues that we will address in the following sections. Another nuance is that for some objects the main spec-z catalogue contains multiple measurements made with different instruments, and in some cases these spec-z values have large residuals between each other (> 0.1). At this stage we do try to determine which measurements are correct, neither discard these objects. Instead, during the crossmatch, we simply use the spec-z measurements that are the best coordinate match to the COSMOS2015 objects. In § 4.1 we analyse these objects to clarify the nature of the photo-z outliers.

The resulting dataset is cross-matched with the COSMOS2015 photometric catalogue, obtaining $\sim 20,000$ objects (the exact amount depends on the bands involved for limiting photometric errors, varying in the various experiments; see § 2.4). The pre-processing does not noticeably affect the spec-z distribution for $z_{\text{spec}} \leq 4$. However, the number of objects for $z_{\text{spec}} > 1.2$ is approximately one order of magnitude lesser than the amount of closer objects (see Fig. A.1 in Appendix A for the redshift distributions before and after the cleaning). In absolute numbers, we have only ~ 700 galaxies in the redshift range $1.2 < z_{\text{spec}} < 4$. Such number of objects is not enough to effectively train our photo-z algorithm in this redshift range, and for this reason we limit our further analysis and the resulting catalogue to $z_{\text{spec}} \leq 1.2$.

2.3 DEIMOS spec-z catalogue

Since we want to test our methodology for selecting the subset of photometric data that is well covered by the KB, we need an independent spec-z catalogue different from the main spec-z catalogue selection function. For this purpose, we used the catalogue of spectroscopic redshift presented in (Hasinger et al. 2018), acquired with DEIMOS, within different programs. This catalog provides redshifts for sources that are not included in the main spec-z catalog and that are somewhat fainter (see Fig. 1). For these differences, it represents an excellent benchmark data for this study.

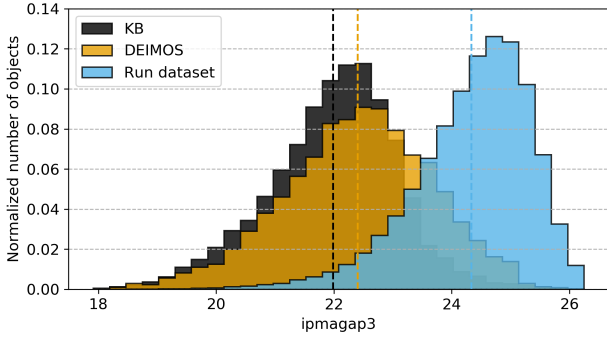


Figure 1. Normalized magnitude distributions for the KB, DEIMOS and run datasets in the `ipmagap3` after standard cleaning but before any SOM filtering. Dashed lines show the mean value of the distribution.

In the preparation of the DEIMOS spec-z catalogue, we follow the same procedure described in § 2.2, aimed at discarding stars, AGNs and unreliable sources².

2.4 Final catalogues and SOM data cleaning prerequisites

After the basic preprocessing described in the previous sections, we produce the following datasets (see Fig. 2):

1. KB (knowledge base), which is the intersection crossmatch between the COSMOS2015 and main spec-z catalogues. It contains both photometry and spec-z. For the ML photo-z experiments we randomly split this KB into train (70% of KB) and blind test (30%) datasets to provide reliable evaluation of the model performance (see Fig. A.3 in Appendix A for the comparison of the model performance on the train and test datasets). To avoid overfitting we also use 10-fold cross validation during the training;
2. Run dataset, which is the COSMOS2015 catalogue after excluding the objects from the KB. It contains only photometric data;
3. DEIMOS dataset, which is an intersection of the run dataset and DEIMOS spec-z catalogue (meaning that it does not contain the objects from the KB). We use the DEIMOS as a control dataset to check how well our cleaning procedures work on independent data, occupying a different hypervolume in the parameter space (see § 2.3).

In order to ensure the quality of the trained model, a reliable photometry is required, so we excluded all objects with high magnitude errors. Some bands have too many objects with unreliable photometry; if applied to these bands, this part of the pre-processing would reduce the size of the dataset by a factor of two or more, and narrow the area of parameter space where the photo-z algorithm would be applicable. To avoid this, we identified the bands affected by too many objects with large magnitude errors ($e_mag > 1$) and excluded them from the experiments. As a rule of thumb this selection was operated by removing bands containing one order higher number of unreliable measurements than the others; these bands are `5_8mag`, `8_0mag`, `NUVmag` and `FUVmag` (see Fig. A.2 in Appendix A). They contain thousands of objects with large

² Note that the DEIMOS catalogue has two different quality flag columns. The one following the same scheme as in Lilly et al. 2009 is labeled "Qf".

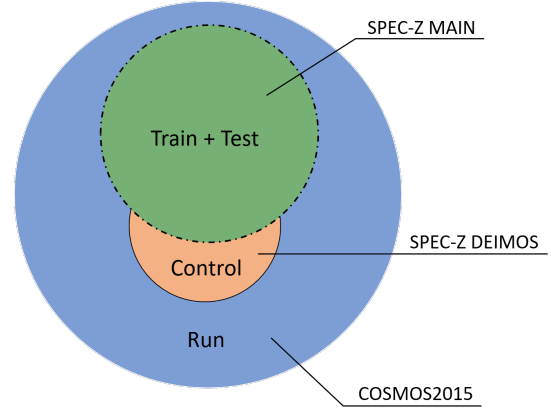


Figure 2. Venn diagram of the catalogues used in this work.

magnitude uncertainties, while the other bands have up to hundreds of such galaxies.

Afterwards, we clean the photometry in the remaining bands, by limiting the magnitude error within the range $0 < e_mag < 1$, where e_mag are magnitude errors for each band. The cleaning is performed for every feature set separately, since it allows us to preserve as many objects as possible (for example, in the experiments where we use only broad bands we do not remove the objects with high magnitude errors in narrow bands). Then in all ML experiments we independently normalize each band to the $[0, 1]$ range.

In order to take care of the mentioned low extrapolative power of ML models, we have to make sure that the run dataset is compliant with the KB in terms of parameter space coverage. Fig. 1 shows the magnitude distribution for the KB, DEIMOS and run datasets in `ipmagap3`. As it can be seen, our run dataset is noticeably deeper than the KB and DEIMOS datasets, as expected due to the spectroscopic bias induced by the targeting algorithms.

We then limit the magnitudes in the run dataset bands by their corresponding maximum values present within the KB. However, this is just a preliminary solution, since it does not guarantee a full similarity between the KB and run datasets, with respect to the parameter space. In § 3.5 we introduce a more accurate procedure to align the run dataset to the parameter space of the KB.

The summary on the parameters of the datasets used in this work (except the preliminary experiments to determine the optimal feature set, described in § 4.1) is given in Tab. 1.

3 METHODS

In this work, we use two neural network algorithms. To calculate the photo-z point estimations, we use the supervised ML algorithm MLPQNA (Brescia et al. 2013, 2014). Furthermore, in order to investigate and clean the datasets, we use an unsupervised ML approach, based on a modified version of the well-known dimensionality reduction algorithm SOM (Kohonen 2013).

3.1 MLPQNA algorithm

MLPQNA is a neural network based on the classical Multi-layer Perceptron with two hidden layers (Rosenblatt 1963). Instead of the standard Backpropagation learning rule this algorithm uses a more sophisticated Quasi Newton approximation of the Hessian error matrix (Nocedal 2006). MLPQNA was successfully used for

Dataset	Size	spec-z range	Median spec-z	imagap3 range	Median imagap3
KB	19893	[0.020; 1.2]	0.57	[17.91; 26.19]	22.02
DEIMOS	2288	[0.025; 5.68]	0.89	[18.48; 25.90]	22.93
Run	228361	NA	NA	[18.14; 26.25]	24.49

Table 1. Main spectroscopic properties of the datasets. For the initial set of experiments, described in § 4.1, different sets of bands were used. The filtering of the objects with large magnitude errors was performed for each feature set independently (see § 2.4), meaning that the exact parameters of the datasets were varying from experiment to experiment. However, these variations were small (e.g. the variations of the sizes of the datasets were less than 1%). The parameters given in this table describe the dataset with an optimal feature set, which was determined in § 4.1 and then used throughout the rest of the paper.

Parameter name	Parameter value
decay	0.001
restarts	80
threshold	0.01
epochs	20000
activation function	tanh
nHiddenLayers	2
number of neurons in the first layer	(2-num_features)+1
number of neurons in the second layer	num_features - 1
cost function	Mean squared error

Table 2. MLPQNA model hyper-parameters settings (see Brescia et al. 2013 for the details).

photo-z estimation in a number of papers (such as, Biviano et al. 2013, Nicastro et al. 2018, Brescia et al. 2013, 2014, Cavuoti et al. 2012a,b, 2015a, 2017a,b).

The model hyper-parameters were heuristically selected on the basis of our past experience and on an intensive test campaign. To determine the number of neurons in each layer, we follow the rule of thumb described in Brescia et al. (2013). This rule implies that the optimal number of neurons for the first hidden layer equals $2N + 1$ and the optimal number of neurons in the second hidden layer is $N - 1$, where N is number of features (i.e., photometric bands). The MLPQNA hyper-parameters are reported in Tab. 2.

3.2 Metrics

In order to evaluate the quality of photo-z estimations, we calculate the residuals as:

$$\Delta z = \frac{z_{\text{spec}} - z_{\text{phot}}}{1 + z_{\text{spec}}} \quad (1)$$

and apply the following set of statistical metrics:

1. Standard deviation $\sigma(\Delta z)$;
2. Normalized median absolute deviation $\text{NMAD}(\Delta z) = 1.48 \times \text{median}(|\Delta z|)$, which is less sensitive to catastrophic outliers than $\sigma(\Delta z)$;
3. Bias, defined as $\text{mean}(\Delta z)$;
4. Percentage of outliers $\eta_{0.15}$, defined as a number of sources with $|\Delta z| \geq 0.15$.

3.3 SOM

The Self Organizing Map (SOM) is a neural network algorithm first described in Kohonen (1982). The idea behind SOM is the following: a parameter space of an arbitrary dimensionality is projected on a map of lesser dimensionality, most commonly 2-dimensional, in such a way that neighbour instances in the original parameter space remain neighbours on the resulting map. For this purpose, the SOM algorithm compares the feature vector of every object in the dataset (in our case the magnitude vector of every galaxy) with the weight vector of the same dimensionality associated with each cell on the 2D map. The object is then placed in the cell having the most similar weight vector (in terms of euclidean distance). Such cell is called Best-Matching Unit (BMU). The weights of the BMU and its neighbour cells are updated in such a way that they become more similar to the feature vector of the object. This mechanism ensures that, at the end of training loop, the map learns the representation of the parameter space of the entire training dataset in a self-organized way. That is why SOM is commonly used to perform an unsupervised data exploration. In photo-z estimation applications, several authors demonstrated that SOM can be used for different tasks. For example, Geach (2012) and Way & Klose (2012) used it to obtain photo-z, while Carrasco Kind & Brunner (2014) applied it to estimate photo-z PDFs. Finally, Masters et al. (2015) adapted the SOM to check the coverage of the photometric parameter space by a given spectroscopic sample, thus indirectly creating a suitable method to optimize a spectroscopic follow-up strategy.

In this work we use the SOM for two different purposes: i) to detect potentially unreliable spec-z in the KB (see Sect. 3.4 and 4.2); ii) to ensure that the run dataset occupies the same part of the parameter space as the KB, i.e. to remove objects in the run dataset that are photometrically different from those in the KB (see Sect. 3.5 and 4.3). In our experiments we use a modified version of MiniSOM (Vettigli 2018)³.

We use photometric bands as the input features for the SOM training. To analyse the datasets, we colour-label the resulting maps using either photo-z, spec-z, or the number of objects within each cell (also called the cell’s occupation). The latter mapping is further referred as occupation maps, and it allows us to check how well the dataset, used for the labelling, covers the parameter space of the SOM training dataset.

Most of the SOM hyper-parameters (specifically, number of epochs, sigma, learning rate and neighbourhood function) are chosen via grid search. Their final values are listed in Tab. 3. The choice of the shape (either square, rectangular or spherical) of the maps is

³ The original version of MiniSOM can be found in the repository <https://github.com/JustGlowing/minisom>. Our modified version is available at <https://github.com/ShrRa/minisom>.

Parameter name	Parameter value
width (low-resolution SOM)	25
height (low-resolution SOM)	28
width (high-resolution SOM)	67
height (high-resolution SOM)	64
num_features	10
epochs	6000
sigma	5
learning rate	0.5
neighborhood_function	bubble

Table 3. SOM settings used for all experiments in this study. For more details about low and high resolution maps, see § 3.3.

somewhat arbitrary; in a number of previous papers different shapes were tried and proven to be useful (see e.g. Buchs et al. 2019, Carasco Kind & Brunner 2014, Masters et al. 2015). We opted for rectangular maps, since it is assumed to give the algorithm a preferred direction to align the data Masters et al. (2015). It is worth noticing, though, that in the preliminary experiments we did not see any significant effect of the shape of the maps on the analysis, described in the next sections.

The size of the map is chosen in such a way that, on average, each cell contains more than 30 galaxies from the training set. The choice of this size is based on the best compromise between the two competing goals: the reliability of statistics within each cell, and the need to capture the data topology with the maximum finesse. A SOM with a small number of cells provides us a higher number of galaxies per cell, thus improving the reliability of the statistical indicators. On the other side, a larger SOM shows more details of the data distribution in the parameter space, but the statistics within some cells become unreliable. For this reason, we use SOM of different sizes. Specifically, we use small low-resolution maps to determine the anomalous sources within each cell, and large high-resolution maps to investigate the train dataset coverage of the parameter space defined by the run catalogue.

3.4 Spec-z cleaning with SOM

The trained SOM places objects with similar feature vectors in the same or neighbour cells. If some object has a photometry-spec-z relationship that appears to be anomalous for its BMU, such object will be considered as an outlier in terms of spec-z distribution of this BMU. In order to avoid the potential confusion between these in-cell outliers with the traditional outliers of a photo-z distribution, hereafter we will refer the in-cell outliers as *anomalous sources* or *anomalies*.

We assume that these objects have a lower photo-z reliability, so we drop them out. In order to exclude such objects, for every galaxy we calculate the coefficient:

$$K_{\text{spec}} = \frac{\left\langle z_{\text{spec}}^{\text{BMU}} \right\rangle - z_{\text{spec}}^{\text{obj}}}{\sigma(z_{\text{spec}}^{\text{BMU}})} \quad (2)$$

where $\left\langle z_{\text{spec}}^{\text{BMU}} \right\rangle$ is the mean spec-z obtained by averaging over the objects falling in the same BMU, $z_{\text{spec}}^{\text{obj}}$ is the spec-z of the galaxy,

and $\sigma(z_{\text{spec}}^{\text{BMU}})$ is the standard deviation of the spec-z distribution within the BMU cell. This coefficient has the same meaning as a standard score, or Z-score, often used in statistics. We choose the prefix K instead of Z to avoid confusion with redshifts. Typically, objects are considered to be outliers if $|K_{\text{spec}}| > 3$. Yet, in our experiments we also tried other criteria to see how it affects the photo-z quality (see § 4.2).

3.5 Parameter space verification with SOM occupation map

As we pointed out earlier, neural networks cannot perform extrapolation. It means that, in order to obtain reliable results, the run dataset has to occupy the same area of the parameter space that is well sampled by the KB. Fig. 1 shows that, in terms of magnitude distribution, our train and run datasets are quite different. Therefore, in order to avoid biasing, we need to estimate the statistics for each magnitude bin independently. Furthermore, in order to obtain reliable results, we have to keep the parameter space of the run dataset as similar as possible to the parameter space of the KB. Usually this is done by limiting the magnitudes of the run dataset to the maximum magnitudes of the KB, i.e. by cutting the faint-end "tail" of the magnitude distributions (e.g. Cavuoti et al. 2015b, Wright et al. 2019, Eriksen et al. 2019). But this approach poses a major problem: if extreme cuts are adopted, the coverage of the parameter space is ensured but at the risk of losing many objects with reliable photo-z. With a soft limiting value, on the other hand, the run dataset is affected by too many objects that lay outside of the KB parameter space.

Using SOM occupation maps, it is possible to implement a more accurate method of photometry filtering, based on the approach first investigated by Masters et al. (2015). The idea behind the method is simple: we train the SOM on the run dataset and then project the KB on the trained map. Since the entire SOM represents a projection of the parameter space of the run dataset, the galaxies in the KB will be clustered only in a subset of cells, with a fairly large number of cells either poorly occupied or completely empty. For these cells we do not have spectral information and hence photo-z predictions cannot be trusted. In order to capture in detail the coverage of the run dataset parameter space by the KB, we use a high-resolution SOM map of size 67X64 (Tab. 3).

4 EXPERIMENTS

The experimental part of this work consists of four stages:

1. The first one, described in § 4.1, is dedicated to identifying the optimal parameters for MLPQNA. For these experiments, we use our KB with only the standard pre-processing, as outlined in § 2.
2. The second set of experiments is described in § 4.2. It aims to analyse how effective is our SOM in removing sources with anomalous spec-z. In this set of experiments we also use only the KB.
3. At the third stage, discussed in § 4.3, we check whether the SOM can be used to extract from a new dataset (DEIMOS) only those sources that belong to the same part of the parameter space as the KB, i.e. photometrically similar to the sources from the KB. For this set of experiments we use both the KB and the DEIMOS datasets.
4. Finally, in § 4.4 we apply the developed methods to estimate

the photometric redshifts and their reliability for objects in the run dataset.

4.1 Photo-z before SOM cleaning

Here we calculate the photometric redshifts for the KB after the standard pre-processing described in §2. We performed a number of experiments with different combinations of features, namely: all photometric bands, only broad bands, broad bands plus one or more narrow bands, with five "SDSS-like" bands, etc. The results of the most representative experiments are reported in Tab. 4.

Keeping in mind that COSMOS2015 has exceptionally rich and well-calibrated photometry, one could expect to obtain photo-z catalogue of high precision. Our expectations were also based on the very precise results obtained with SED fitting in Laigle et al. (2016), and on the fact that in previous works (e.g. done for SDSS-DR9 (Cavuoti et al. 2017b) and KiDS (Brescia et al. 2014)), MLPQNA generally performed on a comparable or better level than other photo-z algorithms.

Yet, in all the experiments, reported in Tab. 4, we did not reach the accuracy achieved in previous works. In particular, we have noticeably higher $\sigma(\Delta z_{ML})$ and percentage of outliers than those reported in the aforementioned papers for KiDS and SDSS-DR9.

The COSMOS2015 is deeper than the catalogues used in those publications, so the cause of the deterioration of the overall statistics could be in the lower quality of photometry and spectroscopy for the high-z sources. But even for low-z galaxies (i.e. with $z_{spec} < 0.5$), both the percentage of outliers and $\sigma(\Delta z_{ML})$ turned out to be of lower quality (see Tab. 5). In fact, there is an unexpected high percentage of outliers in all redshift bins; they are also uniformly distributed across the whole observed field, meaning that photo-z errors are not caused by the contamination by the light of some nearby star. Also, various feature sets show similar percentage of outliers, so it is unlikely that the source of the problem is the calibration of photometry in some particular band.

Another possible explanation is that the photo-z outliers can be either misinterpreted spectra (in a broad sense of this word, i.e. including blended galaxies, incorrect crossmatch between photometric and spectroscopic catalogues, etc.) or exotic objects. Thanks to the fact that some objects in our main spec-z catalogue contain more than one spec-z measurement, we can estimate how many of the outliers belong to each of these categories. In order to do this, we select objects with more than one measurement of spec-z and calculate maximum difference between these measurements, calling it spec-z scatter. Then we calculate the percentage of outliers separately for objects with a single spec-z measurement, multiple measurements and small (< 0.1) scatter, and multiple measurements and large (≥ 0.1) scatter. Tab. 6 reports these calculations for ML and SED fitting photo-z.

From this table we can deduce several facts:

1. For the objects with multiple spec-z values the percentage of outliers for ML and SED fitting photo-z is essentially the same.
2. For the objects with small spec-z scatter this percentage is significantly lower ($\eta_{0.15} \sim 0.2\%$) than for the objects with large spec-z scatter ($\eta_{0.15} \sim 11\%$).
3. For the objects with single spec-z measurement the percentage of outliers for SED fitting is $\sim 50\%$ higher than for ML.

The most probable explanation here is that for the photo-z outliers with large spec-z scatter, the specific spec-z measurement used to estimate the photo-z residual is incorrect. Consequently, the

majority of such bona fide outliers are likely to have correct photo-z predictions. It also implies that a significant percentage of bona fide outliers with single spec-z measurements should be attributed to incorrect spec-z measurements. At the same time, we should not assume that the percentage of incorrect spec-z measurements in this group is the same as for the objects with multiple measurements, since there is no guarantee of similarity of the selection functions for these two categories of objects.

Instead, we use the SOM cleaning procedure, described in § 3.4, to select a set of objects with reliable spec-z even without multiple spec-z measurements.

4.2 Photo-z statistics after removing in-cell anomalous spec-z

We train the SOM, using the KB with the set of broad bands that gave us the best results for the MLPQNA experiments (u, B, V, r, ip, zpp, Y, J, H, Ks, see Tab. 4). This feature set can be viewed as an approximation of the feature set that will exist for the combined LSST and Euclid data, which will also range from optical to NIR wavelengths (Rhodes et al. 2017). Fig. 4 shows the resulting SOM map, color-labelled with, respectively, the mean and standard deviation of spec-z and ML and SED fitting photo-z. In order to discard objects with anomalous spec-z values, we calculate the in-cell spec-z outlier coefficients K_{spec} for each source, as defined in Eq. (2); then we bin the whole KB according to the value of this coefficient and calculate the statistics of photo-z residuals for each bin. This allows us to check how the quality of photo-z correlates with similarity between the spec-z of a given source and the mean spec-z of its BMU.

Fig. 3 shows that the majority of the objects have relatively small K_{spec} (second row of the figure), and the statistics are much better for them than for the objects with larger absolute values of K_{spec} . In the majority of the bins ML photo-z's have lower standard deviations (third row from the top) and lower percentage of outliers (last row from the top) than SED photo-z's, but higher NMAD (fourth row). Predictably, mean residuals (second row from the bottom) have inverse correlation with K_{spec} , implying that photo-z predictions, for objects with spec-z lower than the median spec-z of their BMU, are biased towards higher values, and vice versa.

By limiting our dataset to galaxies with absolute value of K_{spec} smaller than 1, we reduce the percentage of outliers from 1.64 to 0.19 for ML photo-z and from 2.23 to 0.7 for SED fitting. The standard deviation of residuals also is reduced by a factor ~ 2 (see Tab. 7).

Remarkably, after this cleaning the statistics are effectively the same as for the objects with multiple spec-z measurements and low spec-z scatter. In other words, removing in-cell anomalous spec-z leaves us with a reliable set of spec-z with no need to use repeated spec-z measurements, and this set is twice as large as the one with multiple measurements.

The lower part of Tab. 6 shows that while the percentage of outliers for the ML photo-z drops not only for the objects with large spec-z scatter, but for other categories as well, for the SED fitting the improvement for the objects with single spec-z measurement is weaker.

Taking into account that the run dataset does not contain spec-z, it appeared useful to check whether the quality of the dataset could be improved by using photo-z in-cell anomaly detection instead of spec-z. To do so, we calculated outlier coefficients for SED and ML photo-z (K_{SED} and K_{ML} correspondingly), and applied the same filtering using these coefficients instead of K_{spec} . It turns out

Exp ID	Description	bands	Mean	$\sigma_{\Delta z/(1+z)}$	NMAD	$\eta_{0.15}$
exp001	SDSS-like, aper2	u,B,r,ip,zpp	0.000	0.053	0.025	1.999
exp002	SDSS-like, aper3	u,B,r,ip,zpp	-0.001	0.051	0.027	1.807
exp003	SDSS-like, aper_auto	u,B,r,ip,zpp	-0.003	0.055	0.027	2.364
exp004	SDSS-like, aper_ISO	u,B,r,ip,zpp	-0.004	0.059	0.028	2.346
exp005	broad bands, aper2 and aper3	u,B,r,ip,zpp	-0.001	0.051	0.025	1.756
exp006	broad bands, aper3	B,H,J,Ks,V,Y,ip,r,u,zpp	-0.002	0.048	0.018	2.138
exp007	broad bands + one narrow band, aper3	B,H,J,Ks,V,Y,ip,r,u,zpp,IB574	-0.002	0.048	0.019	1.642
exp008	all bands, aper3	Ks, Y, H, J, B, V, ip, r, u, zp, zpp, IA484, IA527, IA624, IA679, IA738, IA767, IB427, IB464, IB505, IB574, IB709, IB827, NB711, NB816, Hw, Ksw, yH	-0.002	0.049	0.017	1.877

Table 4. Results of the experiments performed with the trained MLPQNA on the blind test set of the KB, after having just applied the standard KB cleaning procedure.

spec-z bin	Num objects	ML photo-z				SED photo-z			
		$\sigma_{\Delta z/(1+z)}$	NMAD	Mean	$\eta_{0.15}$	$\sigma_{\Delta z}$	NMAD	Mean	$\eta_{0.15}$
[Overall]	5967	0.048	0.019	-0.0023	1.64	0.094	0.011	-0.0041	2.23
[0.0; 0.2]	422	0.100	0.027	-0.0416	8.29	0.278	0.012	-0.0552	7.82
[0.2; 0.4]	1445	0.043	0.016	-0.0081	1.31	0.056	0.008	-0.0034	1.94
[0.4; 0.6]	1158	0.038	0.016	0.0003	1.04	0.067	0.010	-0.0002	2.07
[0.6; 0.8]	1489	0.036	0.018	0.0001	1.01	0.052	0.012	0.0002	1.48
[0.8; 1.0]	1085	0.032	0.019	0.0041	0.55	0.044	0.014	0.0057	1.20
[1.0; 1.2]	368	0.051	0.028	0.0292	2.99	0.094	0.027	-0.0068	3.53

Table 5. Statistics for the test set calculated in spec-z bins. ML photo-z used here were obtained during the exp007 from Tab. 4 using ten broad and one medium bands.

Case	Num objects	ML photo-z		SED photo-z	
		Num outliers	% outliers	Num outliers	% outliers
Total	5967	98	1.64	133	2.23
Single measurement	3745	63	1.68	98	2.62
Multiple measurements, spec-z scatter <0.1	1945	4	0.21	5	0.26
Multiple measurements, spec-z scatter ≥ 0.1	277	31	11.19	30	10.83
$ K_{\text{spec}} \leq 1$, total	4311	8	0.19	30	0.70
$ K_{\text{spec}} \leq 1$, single measurement	2683	5	0.19	24	0.89
$ K_{\text{spec}} \leq 1$, multiple measurements, spec-z scatter <0.1	1468	0	0.00	1	0.07
$ K_{\text{spec}} \leq 1$, multiple measurements, spec-z scatter ≥ 0.1	160	3	1.88	5	3.12

Table 6. Statistics for ML and SED outliers for the test set of the KB for objects with different number and scatter of spec-z measurements. The upper part of the table reports the results before removing in-cell spec-z anomalies, the lower four rows report the results after $|K_{\text{spec}}| \leq 1$ filtering.

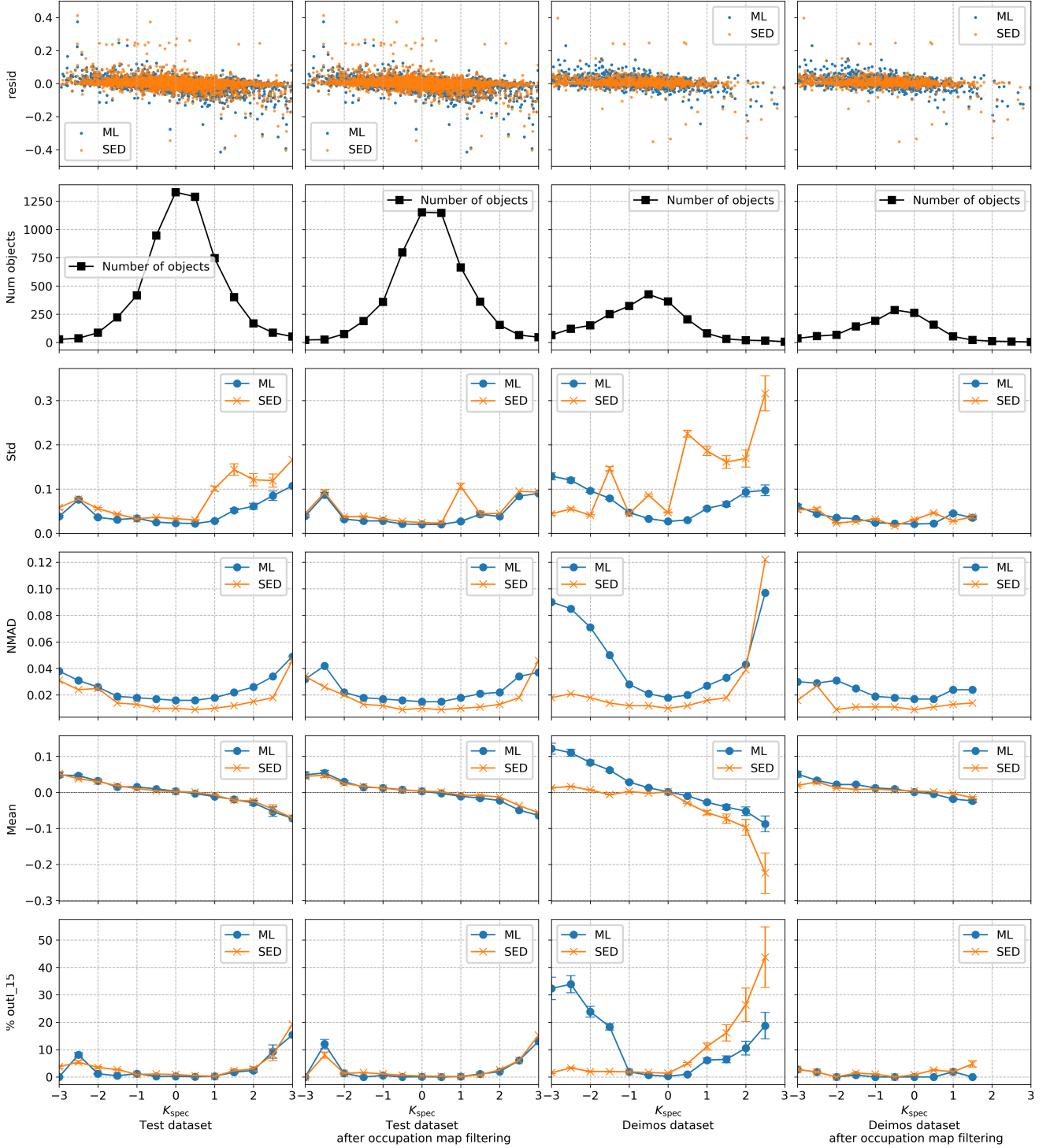


Figure 3. Statistics for the test and DEIMOS datasets in K_{spec} bins before and after occupation map filtering. Bins with number of objects < 15 are considered to be unreliable and excluded from these plots.

that such filtering improves the overall statistics, even though less than the K_{spec} cleaning (upper half of Tab. 7). As expected, the relative improvements are stronger for the SED fitting photo- z than for the ML photo- z ; in § 5.3 we will discuss this aspect in better detail.

4.3 Photo- z after parameter space verification with occupation map

In order to be able to discard the part of the run dataset for which MLPQNA predictions are not likely to be reliable, we have to use occupation maps to identify and flag galaxies that are not photometrically similar to the galaxies of the train dataset. To estimate

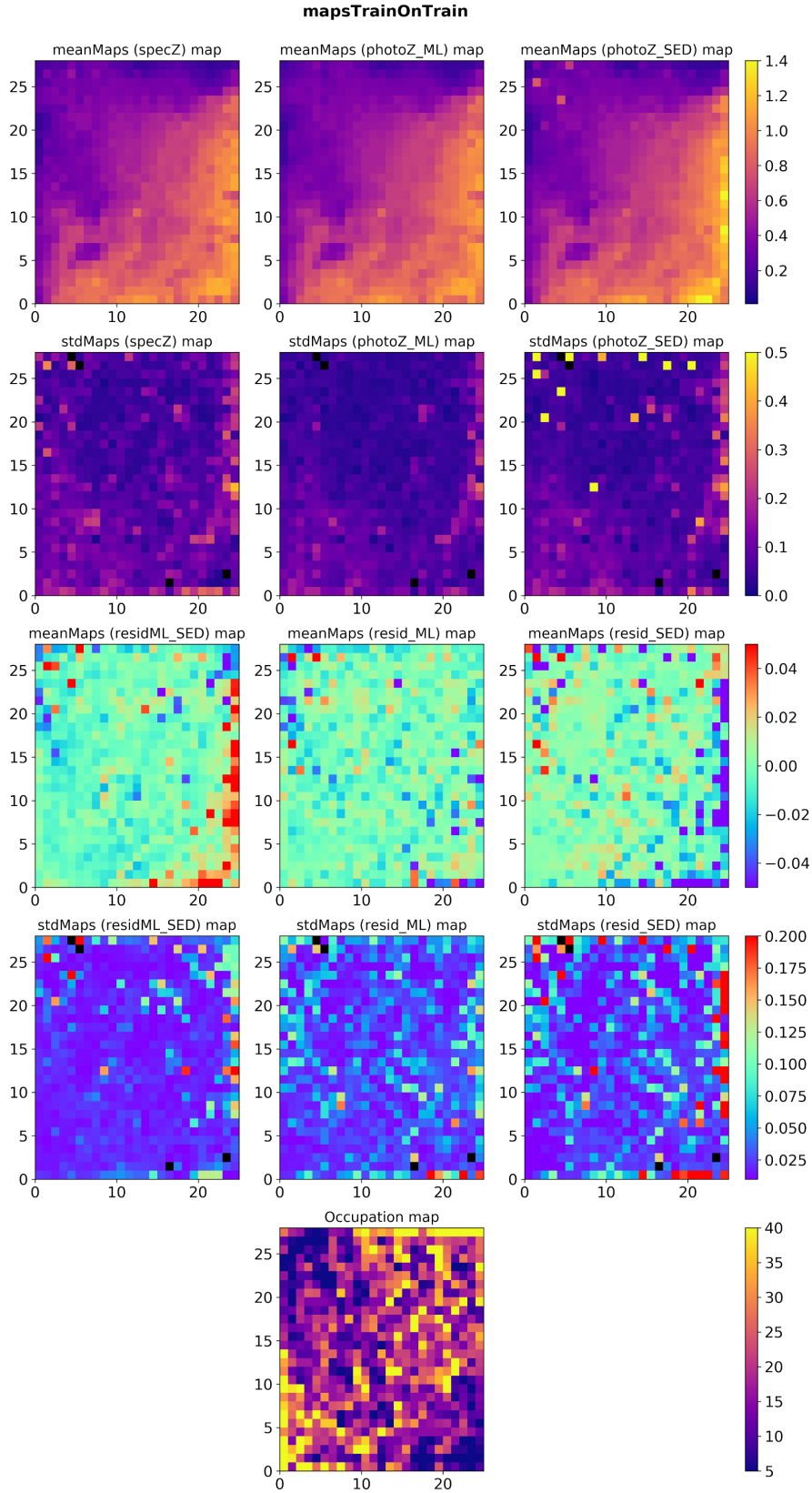


Figure 4. SOMs built and labelled with KB. The first two rows from the top illustrate mean and standard deviation of the redshifts (spectroscopic on the left, ML in the center and SED fitting on the right) within each cell. The third and fourth rows illustrate mean and standard deviation of residuals: on the left are the maps calculated for the residuals between ML and SED fitting photo-z, in the center and on the right are the residuals for ML and SED fitting photo-z. The last plot reflects how many objects are within each cell. Black cells on the occupation and mean maps imply that these cells are empty. On the maps of standard deviation black cells mean that occupation of the cell equals 1 and standard deviation cannot be calculated.

Filtering	Num objects	ML photo-z				SED photo-z			
		$\sigma_{\Delta z}$	NMAD	Mean	$\eta_{0.15}$	$\sigma_{\Delta z}$	NMAD	Mean	$\eta_{0.15}$
No filtering	5967	0.048	0.019	-0.0023	1.64	0.094	0.011	-0.0041	2.23
$ K_{\text{spec}} \leq 1$	4311	0.025	0.017	0.0002	0.19	0.052	0.010	0.0006	0.70
$ K_{\text{ML}} \leq 1$	4071	0.045	0.018	-0.0020	1.28	0.077	0.010	-0.0026	1.65
$ K_{\text{SED}} \leq 1$	4133	0.043	0.018	-0.0020	1.06	0.061	0.010	-0.0021	1.43
trainMapOccupation > 5	5167	0.041	0.018	-0.0021	1.18	0.058	0.010	0.0001	1.49
$K_{\text{spec}} + \text{trainMapOccupation}$	3761	0.022	0.016	-0.0002	0.05	0.05	0.009	0.0018	0.35
$K_{\text{ML}} + \text{trainMapOccupation}$	3587	0.039	0.017	-0.0015	1.06	0.062	0.010	-0.0003	1.17
$K_{\text{SED}} + \text{trainMapOccupation}$	3624	0.038	0.017	-0.0016	0.94	0.038	0.010	0.0002	0.99

Table 7. Statistics for ML and SED fitting photo-z calculated for the test dataset after different types of filtering. The upper part of the table presents the statistics calculated for the dataset without spec-z and photo-z outliers. The lower part reports the effects of photometric filtering with occupation map.

the performance of such photometry cleaning, we made use of the DEIMOS dataset. Considering that the DEIMOS dataset is slightly deeper than the train dataset, we expect that the cleaning process will mostly remove faint objects. Fig. 5 shows occupation maps for the train, test, DEIMOS and run datasets, respectively. For each object of the test, DEIMOS and run datasets we derive the occupation of its BMU by the galaxies of the train dataset. As expected, Fig. 7 demonstrates that the statistics tend to be better for the cells with higher occupation by the train dataset. Based on the statistics for the DEIMOS dataset (right panel of Fig. 7), we chose to leave only the objects that belong to the cells with occupation > 5, since more strict criteria do not bring further improvements.

Tables 7 and 8 report the overall statistics for the test and DEIMOS datasets, respectively. The statistics are given for the different stages of cleaning, including the cases of combination of cleaning with occupation map and removal of the objects with anomalous spectroscopic or photometric redshifts. From these tables we see that the effect of occupation filtering is much stronger for the DEIMOS than for the test dataset (since the test dataset by construction covers the same regions of the parameter space as the train dataset). Still, even on the test dataset the effect of the filtering with occupation map is comparable or better than the effect of the filtering of the photo-z anomalous sources. Also, occupation map filtering is more cost-effective in a sense that it discards much less objects than spec-z or photo-z anomalous source filtering.

From Tab. 8 we see that without any filtering applied to the DEIMOS dataset, our ML photo-z has worse indicators than SED photo-z. This can be easily understood by remembering that part of the DEIMOS dataset lays outside of the parameter space of the train dataset. But for objects that belong to the cells with good occupation, the percentage of outliers and standard deviations for both ML and SED fitting photo-z are very close.

After additional spec-z anomalous source filtering, the statistics improves even more and reaches approximately the same values as for the KB; the scatter plots in the bottom part of Fig. 6 clearly illustrate the improvement. From there, it can be seen that the two cleaning procedures remove different outliers. The plots for the DEIMOS dataset show that both ML and SED fitting photo-z require occu-

pation map filtering to select the objects with good predictions. Without it, SED fitting produces a lot of catastrophic outliers in the whole range of z_{spec} , and ML systematically fails for the objects with $z_{\text{spec}} > 1.2$. K_{spec} filtering eliminates most of the remaining outliers, distributed randomly across the z_{spec} range.

4.4 SOM cleaning of the run dataset

The COSMOS2015 contains $\sim 500\,000$ galaxies. After the standard pre-processing described in § 2 and excluding objects that belong to the KB, the run catalogue consists of $\sim 190\,000$ galaxies. For all these galaxies we calculate ML photo-z, and in order to determine the reliability of these redshifts, we calculate K_{SED} , K_{ML} and the occupation of their BMU by the objects in the train dataset, as described in the previous subsections.

Since we do not have spec-z for the galaxies in the run dataset, we can only perform an accuracy test comparing SED and ML photo-z. To do so, we construct ML/SED residuals $\Delta z_{\text{ML/SED}} = (z_{\text{SED}} - z_{\text{ML}})/(1 + z_{\text{SED}})$. Obviously, such a test suffers from biases introduced by both photo-z methods, so it can be used only for qualitative estimation of the photo-z robustness.

Tab. 9 compares the statistics for ML/SED photo-z residuals for the DEIMOS and run catalogues after applying different filters. The cleaning with occupation map appears to be the most important step, since it allows to reduce the percentage of outliers by almost an order of magnitude. Removal of SED fitting photo-z anomalous sources also improves the statistics. Maximum improvement for both datasets is achieved by a combination of occupation map filtering and removal of SED fitting photo-z anomalous sources. It reduces the percentage of outliers from 11% to 0.27% for the DEIMOS dataset, and from 40% to 2% for the run dataset. $\sigma(\Delta z)$ for the DEIMOS drops from 0.102 to 0.03, and from 0.238 to 0.056 for the run dataset. NMAD changes from 0.033 to 0.022 for the DEIMOS dataset and from 0.129 to 0.026 for the run dataset.

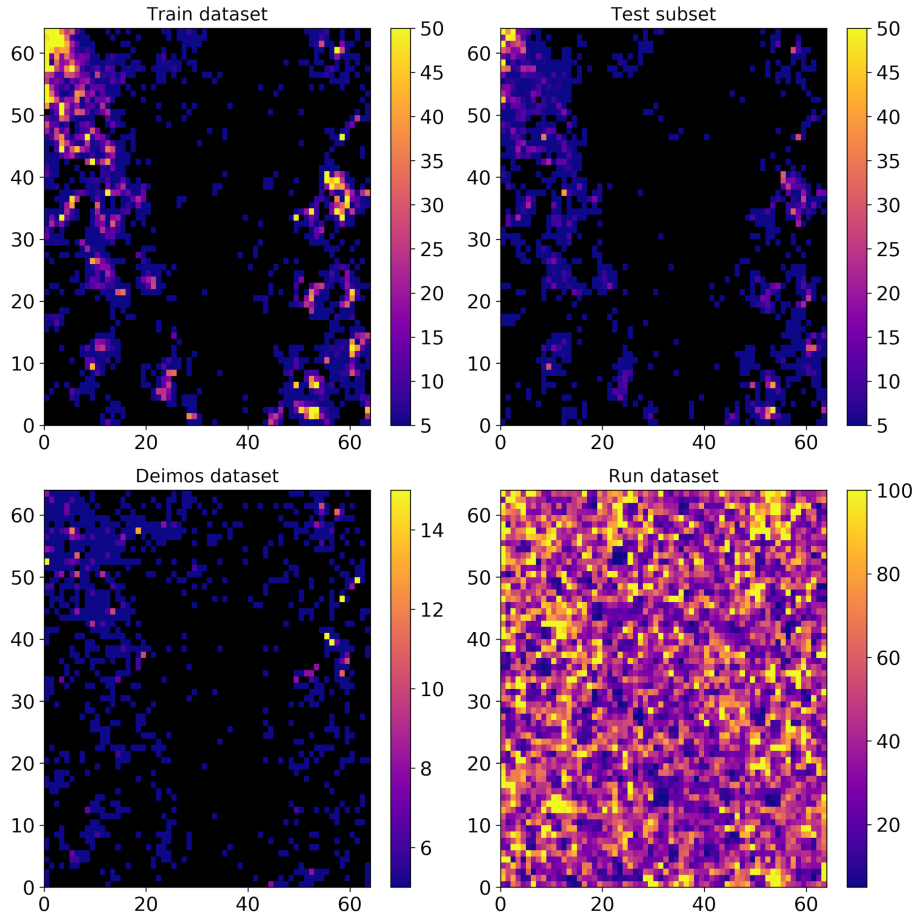


Figure 5. Occupation maps for all datasets projected on SOM trained with run dataset.

Filtering	Num objects	ML photo-z				SED photo-z			
		$\sigma_{\Delta z}$	NMAD	Mean	$\eta_{0.15}$	$\sigma_{\Delta z}$	NMAD	Mean	$\eta_{0.15}$
No filtering	2255	0.099	0.032	0.0347	10.86	0.142	0.014	-0.0082	5.06
$ K_{\text{spec}} \leq 1$	1075	0.035	0.020	0.0018	1.02	0.127	0.011	-0.0103	2.88
$ K_{\text{ML}} \leq 1$	1209	0.095	0.033	0.0392	12.57	0.090	0.013	-0.0031	4.55
$ K_{\text{SED}} \leq 1$	1183	0.085	0.029	0.0245	8.96	0.078	0.013	0.0005	3.30
trainMapOccupation>5	1382	0.058	0.023	0.0127	2.10	0.059	0.012	0.0085	2.68
$K_{\text{spec}} + \text{trainMapOccupation}$	758	0.025	0.018	0.0017	0.13	0.031	0.010	0.0038	0.92
$K_{\text{ML}} + \text{trainMapOccupation}$	724	0.064	0.022	0.0136	1.93	0.060	0.011	0.0080	2.62
$K_{\text{SED}} + \text{trainMapOccupation}$	741	0.046	0.020	0.0063	1.48	0.044	0.011	0.0075	1.89

Table 8. Statistics for ML and SED fitting photo-z for the DEIMOS dataset after different types of filterings. Upper part of the table describes statistics after spec-z and photo-z outlier removal, while the lower part reports the effects of photometry filtering with occupation map.

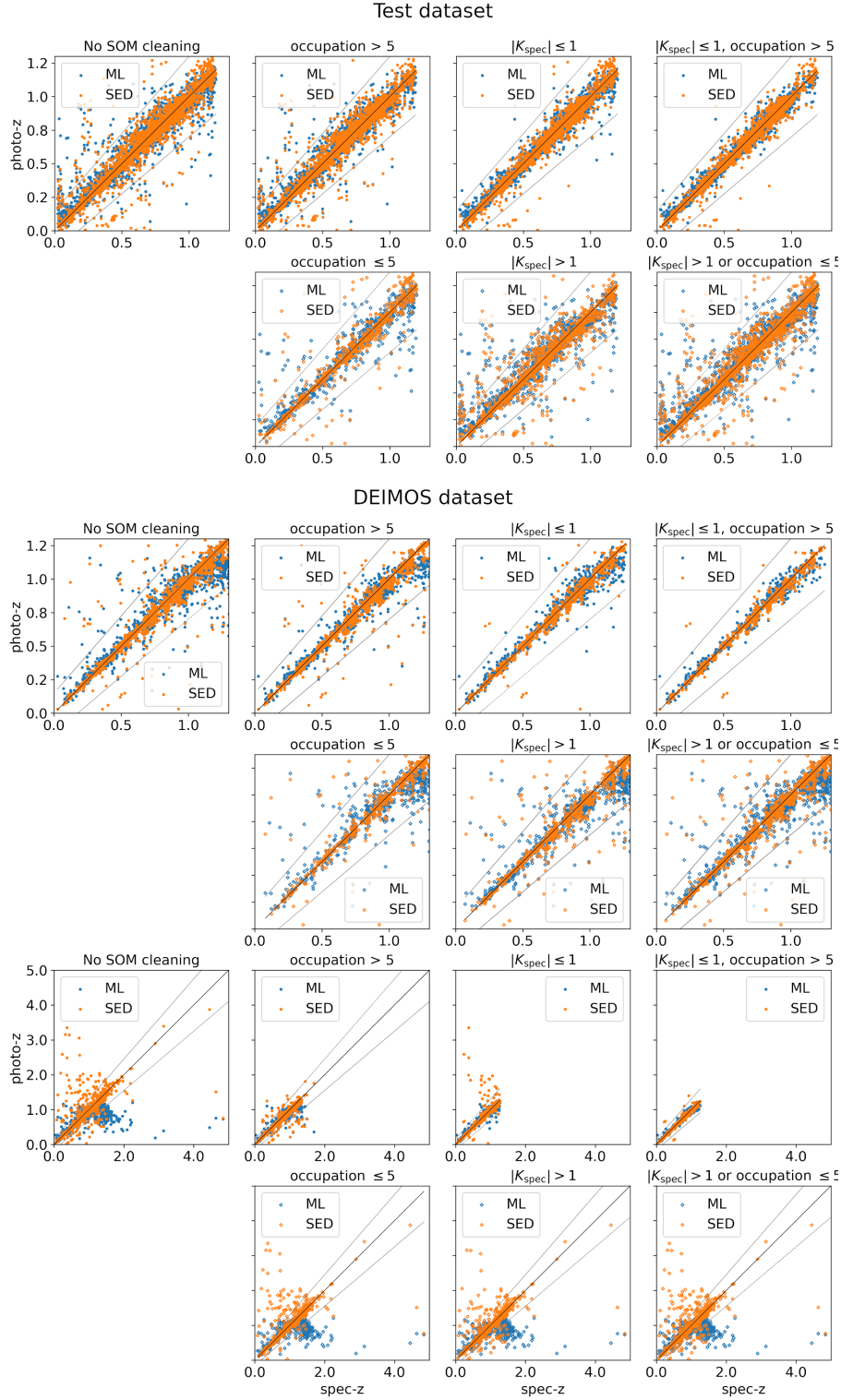


Figure 6. Scatter plots of ML and SED fitting z_{phot} against z_{spec} . In the first column on the left are the datasets before SOM filtering procedures, in the second column are the results after only z_{spec} outlier filtering, in the third are the plots after only occupation map filtering, and in the last column are the datasets after the two cleaning together. The dotted lines show outlier boundaries defined as $z_{\text{photo}} = z_{\text{spec}} \pm 0.15 \cdot (1 + z_{\text{spec}})$. First two rows from the top correspond to the test dataset, the next two rows report the results for the DEIMOS dataset, limited by $z_{\text{spec}} < 1.2$ and $z_{\text{phot}} < 1.2$, the last two rows demonstrate the full DEIMOS dataset ($z_{\text{spec}} < 5$, $z_{\text{phot}} < 5$). In every pair of rows the first row shows the galaxies that remain in the dataset after the filtering, and the second row shows the galaxies that have been removed.

Filtering	DEIMOS dataset					Run dataset				
	Num objects	$\sigma_{\Delta z}$	NMAD	Mean	$\eta_{0.15}$	Num objects	$\sigma_{\Delta z}$	NMAD	Mean	$\eta_{0.15}$
No filtering	2255	0.102	0.033	0.0355	11.35	194509	0.238	0.129	0.1373	40.23
$ K_{\text{spec}} \leq 1$	1075	0.070	0.023	0.0049	2.88	NA	NA	NA	NA	NA
$ K_{\text{ML}} \leq 1$	1209	0.088	0.034	0.0392	11.75	137152	0.225	0.110	0.1243	37.76
$ K_{\text{SED}} \leq 1$	1183	0.072	0.030	0.0224	7.44	146773	0.206	0.101	0.1217	34.93
trainMapOccupation>5	1382	0.047	0.023	0.0031	1.52	43279	0.083	0.028	-0.0019	3.59
$K_{\text{spec}} + \text{trainMapOccupation}$	758	0.036	0.020	-0.0028	0.92	NA	NA	NA	NA	NA
$K_{\text{ML}} + \text{trainMapOccupation}$	724	0.043	0.022	0.0048	0.97	33296	0.080	0.028	-0.0029	3.48
$K_{\text{SED}} + \text{trainMapOccupation}$	741	0.030	0.022	-0.0015	0.27	35189	0.056	0.026	-0.0031	2.17

Table 9. Statistics for ML/SED residuals for the DEIMOS and run datasets after different types of filtering. Upper part of the table describes statistics after spec-z and photo-z outlier removal, lower part reports the effects of photometry filtering with occupation map. Taking into account that for the run dataset spectral information is absent, the rows corresponding to spec-z cleanings for run dataset are empty.

4.5 Purely data-driven spec-z sample

Apart from selecting reliable photo-z predictions from the final catalogue, SOM filtering can be used to create a larger and potentially more representative KB. It can be done by including in the KB not only galaxies with 'good' spectral quality flags (see § 2.2), but also those galaxies that have 'non-robust' quality flags, but good SOM quality indicator ($|K_{\text{spec}}| \leq 1$), i.e. those that appear to have typical z_{spec} for their color cell. In practice, it means that we omit the Q_f cleaning and use only $|K_{\text{spec}}| \leq 1$ filtering. The KB constructed in this exclusively data-driven way consists of 24 058 objects instead of 19 893.

For this sample, we calculated photo-z using the same MLPQNA setup as in the previous sections. For additional comparison, we calculated photo-z for a random galaxy sample of the same size, taken from the non-cleaned spec-z dataset. Tab. 10 reports the results of these experiments.

From this table it can be seen that by using only SOM in-cell anomaly filtering, we are unable to obtain the same quality of photo-z as if we make preliminary selection using spectral quality flags. However, for the ML photo-z the difference is rather small; with the combined standard and SOM cleaning, we have $\text{NMAD} = 0.017$ and $\eta_{0.15} = 0.19$, while with SOM-only cleaning $\text{NMAD} = 0.018$ and $\eta_{0.15} = 0.56$; the mean residual is essentially the same for both cases. This deterioration of statistics comes with a benefit of increasing the size of the final spec-z dataset by $\sim 67\%$. SED fitting photo-z show slightly stronger degradation: while NMAD remains of the same order, the mean bias is worsened by two orders, from 0.0006 to -0.0134 , and the percentage of outliers increases from 0.7 to 1.93. The experiment with a random sample taken from the uncleaned spec-z catalogue demonstrates that without any form of data cleaning, photo-z quality is significantly worse.

This purely data-driven selection of reliable spec-z can be suitable not only for photo-z prediction, where larger KB means better representation of the run dataset, but also for a general verification and validation of the quality of spec-z catalogues, useful in other contexts.

5 DISCUSSION

As we have shown in the previous section, there are several ways in which we can apply SOM to improve the quality of the photo-z catalogues. In some cases these cleaning procedures improve both the standard deviation of residuals and the percentage of outliers (e.g. Tab. 8). In this section we compare the effects of the SOM cleaning on ML and SED fitting photo-z (§ 5.1), consider the nature of spec-z and photo-z in-cell anomalies (§ 5.2 and § 5.3), and define general strategies for using the SOM cleaning methodology on other datasets (§ 5.4).

5.1 SED fitting vs. ML

In all the experiments performed on the KB, the ML photo-z distribution has a lower percentages of outliers and lower standard deviations than the SED fitting photo-z distribution, but higher NMAD (see Tab. 7). For the DEIMOS dataset, before SOM filtering, the situation is different: ML photo-z have a significantly higher percentage of outliers ($\sim 11\%$ against 5% for SED fitting), due to the fact that DEIMOS contains many objects laying outside of the boundaries of the parameter space sampled by the KB. Occupation map filtering discards the majority of these outliers and the statistics of both ML and SED fitting photo-z become similar to those for the test dataset (see Tab. 7 and 8). In particular, for ML $\sigma_{\Delta z}$ decreases from 0.099 to 0.058 (for the KB it equals 0.041), and for SED fitting $\sigma_{\Delta z}$ from 0.142 to 0.059 (0.058 for the KB). The percentage of outliers also drops from 10.86% to 2.1% for ML photo-z (1.18% for the KB) and from 5.06% to 2.68% for SED fitting (1.49% for the KB).

The difference between the two methods in terms of NMAD can be explained by the fact that SED fitting methods benefit from the inclusion of the narrow-band photometry. It allows the SED fitting methods to detect emission lines passing through a certain wavelength range (Ilbert et al. 2009). On the contrary, in the case of MLPQNA, the same inclusion of the additional narrow bands does not lead to significant improvements (Tab. 4). Earlier work by several authors (see e.g. Heinis et al. 2016 and Eriksen et al. 2020) demonstrated that inclusion of the narrow-band photometry

Exp ID	Description	Num obj	ML photo-z				SED photo-z			
			$\sigma_{\Delta z}$	NMAD	Mean	$\eta_{0.15}$	$\sigma_{\Delta z}$	NMAD	Mean	$\eta_{0.15}$
exp007	Baseline	5967	0.048	0.019	-0.0023	1.64	0.094	0.011	-0.0041	2.23
exp007-clean	Baseline, $K_{\text{spec}} \leq 1$	4311	0.025	0.017	0.0002	0.19	0.052	0.010	0.0006	0.7
d_exp027	'Dirty' spec-z, $ K_{\text{spec}} \leq 1$	7218	0.033	0.018	-0.0009	0.57	0.135	0.012	-0.0134	1.93
d_exp028	'Dirty' spec-z, random sample	7218	0.072	0.025	-0.0055	4.32	0.178	0.015	-0.0238	5.78

Table 10. Photo-z performance for the test sample with and without standard Q_f cleaning. The first two rows describe baseline exp007 experiment, which was done on the spec-z sample cleaned with standard Q_f criteria (§ 2.2), before and after SOM in-cell spec-z anomaly filtering. The third row describes an experiment done on the spec-z sample that was not cleaned with Q_f, but only with SOM in-cell filtering. The last row reports an experiment done on a random sample from the spec-z catalogue which was not cleaned neither with Q_f nor SOM in-cell filtering.

generally improves ML photo-z only after additional preparations, such as transfer learning or a preliminary extensive phase of feature selection. A possible explanation to this is that in comparison to the broad bands, narrow bands carry redshift signal for a smaller fraction of galaxies, namely, only for those galaxies whose spectrum has emission or absorption lines passing through a particular narrow band. In order to learn to extract this signal, a ML model might need a much larger training set than when only broad bands are used.

Even after occupation map filtering and removing in-cell anomalous spec-z, SED fitting produces a higher number of catastrophic outliers than ML. Also, the residuals for these outliers are larger than for ML outliers (see Fig. 6; for the test dataset the mean absolute value of residuals for SED fitting catastrophic outliers is 0.35, while for ML outliers it's 0.26; for the DEIMOS the mean absolute residual for SED fitting is 0.29, and for ML it's 0.22). As can be seen from the second row of Fig. 4, the SOM map of the standard deviations of SED fitting photo-z has a number of cells with significantly higher values than appear on the $\sigma(z_{\text{spec}})$ and $\sigma(z_{\text{ML}})$ maps. These are the cells where the majority of the catastrophic outliers are located, and it seems likely that these outliers appear due to the lack of a suitable SED template or SED fitting failure.

An unexpected result is that SED fitting seriously benefits from occupation map filtering. For the test dataset, the percentage of outliers drops from 2.23% to 1.49%, while for the DEIMOS it goes from 5.06% to 2.68%, which is even better than what is obtained after spec-z filtering. One possible explanation to this is that the objects in the areas of parameter space that are poorly covered by the spec-z catalogue are likely to be faint and at a high spec-z, thus having a less reliable photo-z due either to the lack of suitable SED templates or to the photometry issues.

The aforementioned results for ML photo-z are obtained using only 10 broad and 1 medium band. In the case of SED fitting photo-z more than thirty (broad, medium and narrow) bands were used; still, the statistics for SED fitting and ML are quite close. It implies some consequences for the observational strategies of the future surveys. Depending on the design of a survey, it can be more beneficial to invest resources into obtaining either a larger spectroscopic KB with ML photo-z algorithms in mind, or additional medium/narrow band photometry for SED fitting. Both decisions lead to similar quality of the photo-z catalogue with some differences in the NMAD and in the percentage of outliers. Obviously, obtaining both an extensive spectroscopic catalogue and medium/narrow band photometry will

allow to use both techniques and to increase the reliability of the photo-z predictions (e.g. Cavuoti et al. 2017b, also see § 5.4).

5.2 Spec-z anomalous sources filtering

Removal of the spec-z anomalous sources drastically reduces the percentage of outliers for both photo-z methods. As we showed in § 4.1, the photo-z outliers mostly appear to be misinterpreted spectra, and removing them from the analysis makes the performance estimation more correct. Yet, there are much more objects with high values of K_{spec} than ML or SED fitting outliers. A question arises, what are all these objects.

Looking at Fig. 3, we can see that in general the statistics (including NMAD, which is less sensitive to hard outliers) deteriorate smoothly with the increase of the absolute value of K_{spec} . This smooth dependency is present not only for ML photo-z, but for SED fitting photo-z as well. It means that within each cell of SOM (which represents a small hyper-volume in the photometric parameter space), both ML and SED fitting perform better for "typical" spec-z than for atypical ones. This is true even for those regions of parameter space that are well-covered by the spec-z catalogue. In other words, K_{spec} works as an additional, finer indicator of whether a given galaxy is well-represented in the spectroscopic KB, although it does not offer any insight on the reasons of why this galaxy is not well-represented - whether it is due to the physical rarity of its type, to the catalogues' selection function or other reasons.

In general, removing objects with high K_{spec} allows us to create a reliable spec-z sample, useful for comparing the performance of different photo-z algorithms. In our case, for the test dataset this sample is more than two times larger than the set of the objects with multiple spec-z measurements that are in good agreement with each other. A purely data-driven approach to the selection of reliable spec-z, described in § 4.5, allows us to enlarge this sample even more, with a comparatively small deterioration of the quality of the data. In every case, the SOM cleaning mostly does not change the overall shape of the redshift distribution of the samples, with an exception of slightly stronger filtering in the lowest and highest redshift bins, where the percentage of outliers is the highest (see Fig. A. 4 and Fig. A. 5 in Appendix A). Consequently, the usage of this method seems to be highly beneficial for the preparation of any future compound spec-z catalogues, and possibly for the verification of the new spec-z surveys against the old ones.

5.3 Photo-z anomalous sources and occupation map filtering

To clean photo-z values for the run dataset, the only possibility is to use K_{ML} or K_{SED} to discard either ML or SED fitting photo-z anomalies. However, the performance is different in the two cases. As it can be seen from Tab. 7 and 8, discarding SED fitting anomalies improves the statistics slightly more than removing ML anomalous sources. Obviously, this is related to the large percentage of outliers obtained in SED fitting photo-z and to their large residuals.

On the DEIMOS dataset, photo-z anomalous sources filtering, together with occupation map cleaning allows to reach $\sigma_{\Delta z} \approx 0.046$ and percentage of outliers $\approx 1.48\%$ for ML photo-z, and $\sigma_{\Delta z} \approx 0.044$ and percentage of outliers $\approx 1.89\%$ for SED fitting. At the same time, for ML/SED residuals on the DEIMOS the same cleaning procedure brings $\sigma_{\Delta z} \approx 0.03$ and percentage of outliers $\approx 0.27\%$, which is quite close to the statistics for ML and SED photo-z after occupation map filtering together with removing spec-z anomalous sources.

In Fig. 8 we plot the values of different statistics in `ipmagap3` magnitude bins at different stages of cleaning of the DEIMOS dataset. As expected, with occupation map cleaning the improvements are mostly achieved due to the filtering in the fainter part of magnitude distribution. Instead of completely losing the faint objects, as it would have happened if we used the traditional cut-off procedure, we are preserving those which have fairly good quality of photo-z predictions. Fig. 9 shows the same picture for the run dataset. For what the standard deviation is concerned, the difference appears for objects fainter than `ipmagap3` ~ 21 , but the most significant effect is observed for objects with `ipmagap3` > 23 .

5.4 Filtering strategies

The optimal strategy of the data cleaning with SOM depends on the nature of a dataset and on the task at hand:

- Identification of spec-z anomalous sources is useful for finding unreliable spec-z and under-represented objects.
- Identification of photo-z anomalies allows us to improve the quality of a photo-z catalogue, especially for SED fitting photo-z. It can be applied to the run catalogue (i.e., for objects without spectral information), but this procedure is effective only for datasets that are well sampled by the KB.
- For the run datasets that are not well sampled by the KB, SOM filtering with an occupation map is the most important step. It leads to significant improvements not only in the case of ML based methods but also in the case of SED fitting.

In this work we use all three types of cleaning with the following thresholds:

1. spec-z anomalies filtering: $K_{\text{spec}} \leq 1$.
2. Occupation map filtering: `trainMapOccupation` > 5 .
3. photo-z anomalies filtering: $K_{\text{SED}} \leq 1$.
4. In cases when better NMAD is needed and percentage of outliers is less critical, SED fitting photo-z are preferable. For the tasks that demand the lowest percentage of outliers, ML photo-z show better results. Finally, it is possible to choose between the two values of photo-z: when photo-z predictions are similar (based on the grid search on the test and DEIMOS datasets we recommend to use the criteria of ML/SED residual < 0.5), it is better to select SED fitting value, and when the residual is > 0.5 , ML photo-z are more likely to be correct. Tab. 11 re-

ports the statistics for photo-z selected in this way for the test and DEIMOS datasets. With such selection we obtain both good NMAD and low percentage of outliers.

6 CONCLUSIONS

In this work, we calculated ML photo-z for the COSMOS2015 catalogue using MLPQNA algorithm. For the training and testing we used multi-instrument spectroscopic KB with $z_{\text{spec}} \leq 1.2$ and various sets of photometric bands, obtaining the best results with a feature set composed by 10 broad and 1 narrow bands. The comparison of the statistics for ML photo-z and SED fitting photo-z, calculated by Laigle et al. 2016 using the whole set of COSMOS2015 bands, showed that ML photo-z has lower percentage of outliers and $\sigma_{\Delta z}$, but higher NMAD. Particularly, for the test dataset without additional SOM cleaning MLPQNA produces photo-z with $\sigma_{\Delta z} = 0.048$, NMAD = 0.019 and $\eta_{0.15} = 1.64\%$, while SED fitting photo-z has $\sigma_{\Delta z} = 0.094$, NMAD = 0.011 and $\eta_{0.15} = 2.23\%$ (Tab. 7).

We found that the ML photo-z algorithm does not benefit from the inclusion of the most medium and narrow photometric bands (Tab. 4). Finding a way to exploit the information contained in those bands should be a subject of further work.

Our experiments demonstrated that a significant percentage of outliers have similar values of ML and SED fitting photo-z. By analysing the objects with multiple spec-z measurements we discovered that the majority of such outliers have unreliable spec-z values, which makes us to believe that the photo-z prediction for these objects are correct and the actual percentage of outliers for both photo-z methods is significantly lower. On the subset of galaxies with multiple similar spec-z measurements, $\eta_{0.15} \sim 0.2\%$ for both photo-z methods.

We tested the possibility of using Self-Organizing Maps (SOM) for removing unreliable spec-z and creating a high-quality spec-z sample. To do this, we calculated a coefficient K_{spec} that quantifies how much a spectrum of a given galaxy differs from the mean spectra of all the galaxies belonging to the same SOM cell, e.g. of the galaxies that are most photometrically similar. We found that K_{spec} allows us to remove objects with incorrect spec-z: the percentage of outliers for the test set of the KB drops from 1.64 to 0.19 for ML photo-z and from 2.23 to 0.7 for SED fitting, and $\sigma_{\Delta z}$ for both ML and SED fitting photo-z improves almost by a factor of ~ 2 (see Tab. 7). At the same time, K_{spec} is sensitive to the intrinsic in-homogeneity of the galaxy population, caused by physical reasons. In this way K_{spec} serves as a fine indicator of whether a given object is well-represented within the KB.

To ensure that our run dataset occupies the same area of the parameter space as the KB, we also used SOM following the methodology that we call *occupation map* cleaning. On the control DEIMOS spec-z dataset, that is slightly deeper than our KB spec-z catalogue, we found that by using this cleaning, we reduce the percentage of outliers from 11% to 2% for ML photo-z and from 5% to 3% for SED fitting photo-z, with consequent improvements of other metrics. The details are reported in Tab. 8.

We find that we can also improve the statistics by excluding the objects with SED fitting photo-z values that are anomalous for their SOM cells. Removing objects with anomalous ML photo-z does not improve the results significantly. Using both occupation map and SED fitting photo-z in-cell anomalies filtering, we are able to bring the statistics for the DEIMOS dataset to the order of those

Photo-z	Test dataset					DEIMOS dataset				
	Num objects	$\sigma_{\Delta z}$	NMAD	Mean	$\eta_{0.15}$	Num objects	$\sigma_{\Delta z}$	NMAD	Mean	$\eta_{0.15}$
ML	3508	0.021	0.016	-0.0001	0.03	725	0.024	0.018	0.0020	0
SED	3508	0.049	0.009	-0.0001	0.06	725	0.027	0.009	0.0022	0.55
Mixed	3508	0.018	0.009	0.0012	0.03	725	0.017	0.010	0.0051	0

Table 11. Statistics for ML, SED fitting and mixed (selected based on the ML/SED residual value) residuals for the test and DEIMOS datasets. Both datasets were cleaned with the following conditions: $\text{trainMapOccupation} > 5$, $|\mathcal{K}_{\text{spec}}| \leq 1$, $|\mathcal{K}_{\text{SED}}| \leq 1$.

for the KB. To be more precise, the standard deviation drops from $\sigma_{\Delta z} = 0.099$ to $\sigma_{\Delta z} = 0.046$ for ML and from $\sigma_{\Delta z} = 0.142$ to $\sigma_{\Delta z} = 0.044$ for SED fitting, and the percentage of outliers lessens from $\eta_{0.15} = 10.86$ to $\eta_{0.15} = 1.48$ for ML and from $\eta_{0.15} = 5.06$ to $\eta_{0.15} = 1.89$ for SED fitting. This result allows us to select the parts of photometric catalogues for which our photo-z predictions, obtained with any algorithm, can be trusted.

All in all, the SOM in-cell anomaly detection, presented in this work, proved to be a viable method for selecting reliable spec-z samples from a contaminated catalogue and a good tool for identifying SED fitting photo-z outliers. The SOM occupation map filtering also seems to be recommendable for ensuring the reliability of the future photo-z catalogues. We plan to investigate the potential of these methods in application to the other kinds of the astronomical datasets in the future works.

7 DATA AVAILABILITY

The source catalogues for this work can be obtained as described in Sect. 2. The final catalogue, containing MLPQNA photo-z and SOM-produced parameters that can be used for selecting objects with high-confidence predictions will be published via CDS Vizier facility. The code for reproducing this work is available in the GitHub repository https://github.com/ShrRa/COSMOS_SOM. The MLPQNA software is available within the PhotoRApToR⁴ (PHOTometric Research APplication To Redshifts Cavuoti et al. 2015a) package.

ACKNOWLEDGEMENTS

We are grateful to the anonymous referee for the suggestions and comments that helped to improve this paper.

This work has received financial support from the European Union's Horizon 2020 research and innovation program under the Marie Skłodowska-Curie grant agreement No. 721463 to the SUN-DIAL ITN network. Stefano Cavuoti acknowledges financial support from FFABR 2017 (Fondo di Finanziamento per le Attività Base di Ricerca). OR thanks Valeria Amaro, Civita Vellucci, Maurizio D'Addona and Kseniia Sysoliatina for useful discussions and technical help at different stages of this research. MB acknowledges financial contributions from the agreement ASI/INAF 2018-23-HH.0, *Euclid* ESA mission - Phase D and the INAF PRIN-SKA 2017 program 1.05.01.88.04.

⁴ http://dame.oacn.inaf.it/dame_photоз.html#photoraptor

REFERENCES

- Arnouts S., Cristiani S., Moscardini L., Matarrese S., Lucchin F., Fontana A., Giallongo E., 1999, *MNRAS*, **310**, 540
- Baldwin J. A., 1977, *ApJ*, **214**, 679
- Ball N. M., Brunner R. J., Myers A. D., Strand N. E., Albers S. L., Tchenguiz D., 2008, *ApJ*, **683**, 12
- Baron D., 2019, arXiv e-prints, p. arXiv:1904.07248
- Baum W. A., 1957, *AJ*, **62**, 6
- Baum W. A., 1962, in McVittie G. C., ed., IAU Symposium Vol. 15, Problems of Extra-Galactic Research. p. 390
- Beck R., Dobos L., Budavári T., Szalay A. S., Csabai I., 2016, *MNRAS*, **460**, 1371
- Benítez N., 2000, *ApJ*, **536**, 571
- Bilicki M., et al., 2018, *A&A*, **616**, A69
- Biviano et al., 2013, *A&A*, **558**, A1
- Bolzoniella M., Miralles J. M., Pelló R., 2000, *A&A*, **363**, 476
- Bonnett C., et al., 2016, *Phys. Rev. D*, **94**, 042005
- Brammer G. B., van Dokkum P. G., Coppi P., 2008, *ApJ*, **686**, 1503
- Brescia M., Cavuoti S., D'Abrusco R., Longo G., Mercurio A., 2013, *ApJ*, **772**, 140
- Brescia M., Cavuoti S., Longo G., De Stefano V., 2014, *A&A*, **568**, A126
- Brescia M., Cavuoti S., Amaro V., Riccio G., Angora G., Vellucci C., Longo G., 2018, *Springer Communications in Computer and Information Science*, **822**, arXiv:1802.07683
- Brescia M., Salvato M., Cavuoti S., Ananna T. T., Riccio G., LaMassa S. M., Urry C. M., Longo G., 2019, *Monthly Notices of the Royal Astronomical Society*, **489**, 663
- Buchs R., et al., 2019, *MNRAS*, **489**, 820
- Butchins S. A., 1981, *A&A*, **97**, 407
- Capak P., et al., 2007, *ApJS*, **172**, 99
- Carrasco Kind M., Brunner R. J., 2013, *MNRAS*, **432**, 1483
- Carrasco Kind M., Brunner R. J., 2014, *MNRAS*, **438**, 3409
- Cavuoti S., Brescia M., Longo G., Mercurio A., 2012a, *A&A*, **546**, A13
- Cavuoti S., Brescia M., Longo G., Mercurio A., 2012b, *A&A*, **546**, A13
- Cavuoti S., Brescia M., De Stefano V., Longo G., 2015a, *Experimental Astronomy*, **39**, 45
- Cavuoti S., et al., 2015b, *MNRAS*, **452**, 3100
- Cavuoti S., Amaro V., Brescia M., Vellucci C., Tortora C., Longo G., 2017a, *MNRAS*, **465**, 1959
- Cavuoti S., et al., 2017b, *MNRAS*, **466**, 2039
- Civano F., et al., 2012, *ApJS*, **201**, 30
- Collister A. A., Lahav O., 2004, *PASP*, **116**, 345
- Connolly A. J., Csabai I., Szalay A. S., Koo D. C., Kron R. G., Munn J. A.,

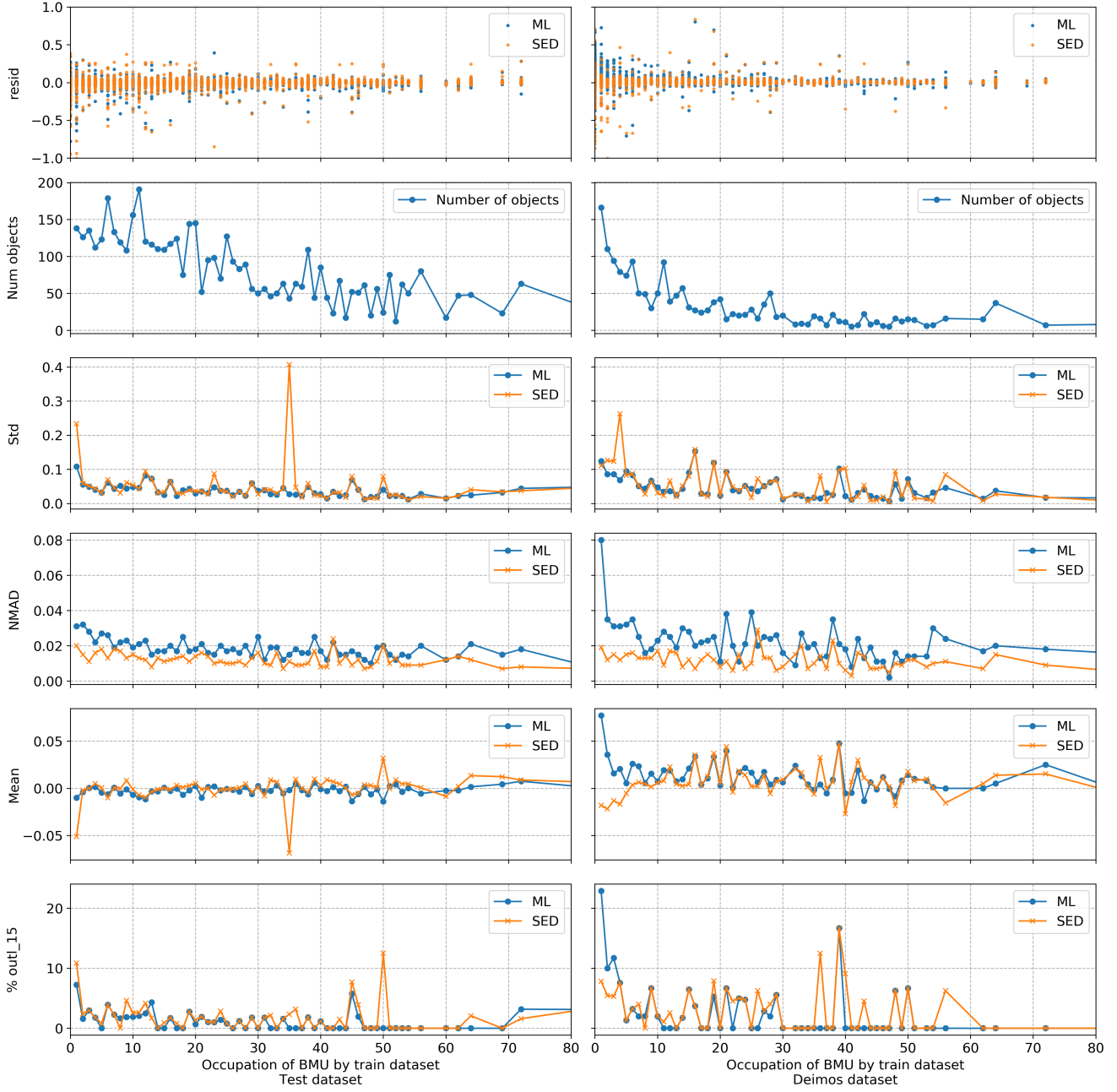


Figure 7. Dependency of the statistics for the test and DEIMOS datasets from the occupation of their BMU by objects from train dataset. The x-axis is limited to occupation ≤ 80 since there are not enough objects in the cells with bigger occupations to calculate reliable statistics.

1995, *AJ*, **110**, 2655
D’Isanto A., Cavuoti S., Gieseke F., Polsterer K. L., 2018, *A&A*, **616**, A97
Donalek C., et al., 2013, arXiv e-prints, p. arXiv:1310.1976
Duncan K. J., Jarvis M. J., Brown M. J. I., Röttgering H. J. A., 2018, *MNRAS*, **477**, 5177
Eriksen M., et al., 2019, *MNRAS*, **484**, 4200
Eriksen M., et al., 2020, *MNRAS*, **497**, 4565
Euclid Collaboration et al., 2020, *A&A*, **644**, A31
Geach J. E., 2012, *MNRAS*, **419**, 2633
Gerdes D. W., Sypniewski A. J., McKay T. A., Hao J., Weis M. R., Wechsler R. H., Busha M. T., 2010, *ApJ*, **715**, 823

Gwyn S. D. J., Hartwick F. D. A., 1996, *ApJ*, **468**, L77
Hasinger G., et al., 2018, *ApJ*, **858**, 77
Heinis S., et al., 2016, *ApJ*, **821**, 86
Hoyle B., 2016, *Astronomy and Computing*, **16**, 34
Ilbert O., et al., 2006, *A&A*, **457**, 841
Ilbert O., et al., 2009, *ApJ*, **690**, 1236
Ivezić Ž., et al., 2019, *ApJ*, **873**, 111
Kohonen T., 1982, *Biological Cybernetics*, **43**, 59
Kohonen T., 2013, *Neural Netw.*, **37**, 52
Koo D. C., 1985, *AJ*, **90**, 418
LSST Science Collaboration et al., 2009, arXiv e-prints, p. arXiv:0912.0201

DEIMOS dataset

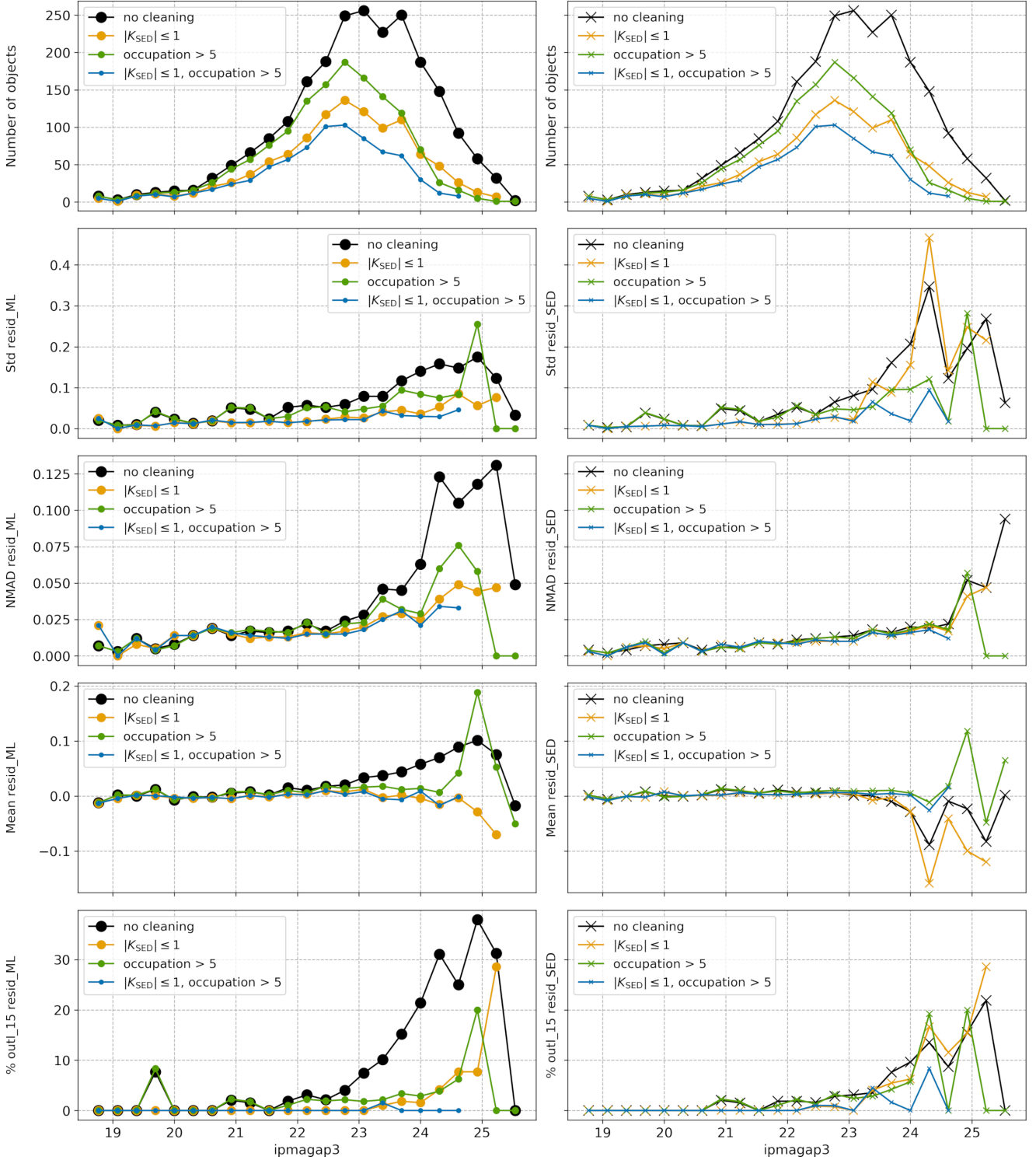


Figure 8. Statistics for the DEIMOS datasets in *ipmagap3* bins after applying different filters. Left panel: ML photo-*z* residuals, right panel: SED fitting photo-*z* residuals. Bins with number of objects < 15 are considered to be unreliable and excluded from these plots.

Laigle C., et al., 2016, *ApJS*, 224, 24

Lanzetta K. M., Fernández-Soto A., Yahil A., 1998, in Livio M., Fall S. M., Madau P., eds, *The Hubble Deep Field*. p. 143 ([arXiv:astro-ph/9709166](https://arxiv.org/abs/astro-ph/9709166))

Laureijs R., et al., 2011, *Euclid Definition Study Report*

([arXiv:1110.3193](https://arxiv.org/abs/1110.3193))

Le Fèvre O., et al., 2005, *A&A*, 439, 845

Lilly S., et al., 2009, *Astronomy & Astrophysics*, 523

Masters D., et al., 2015, *ApJ*, 813, 53

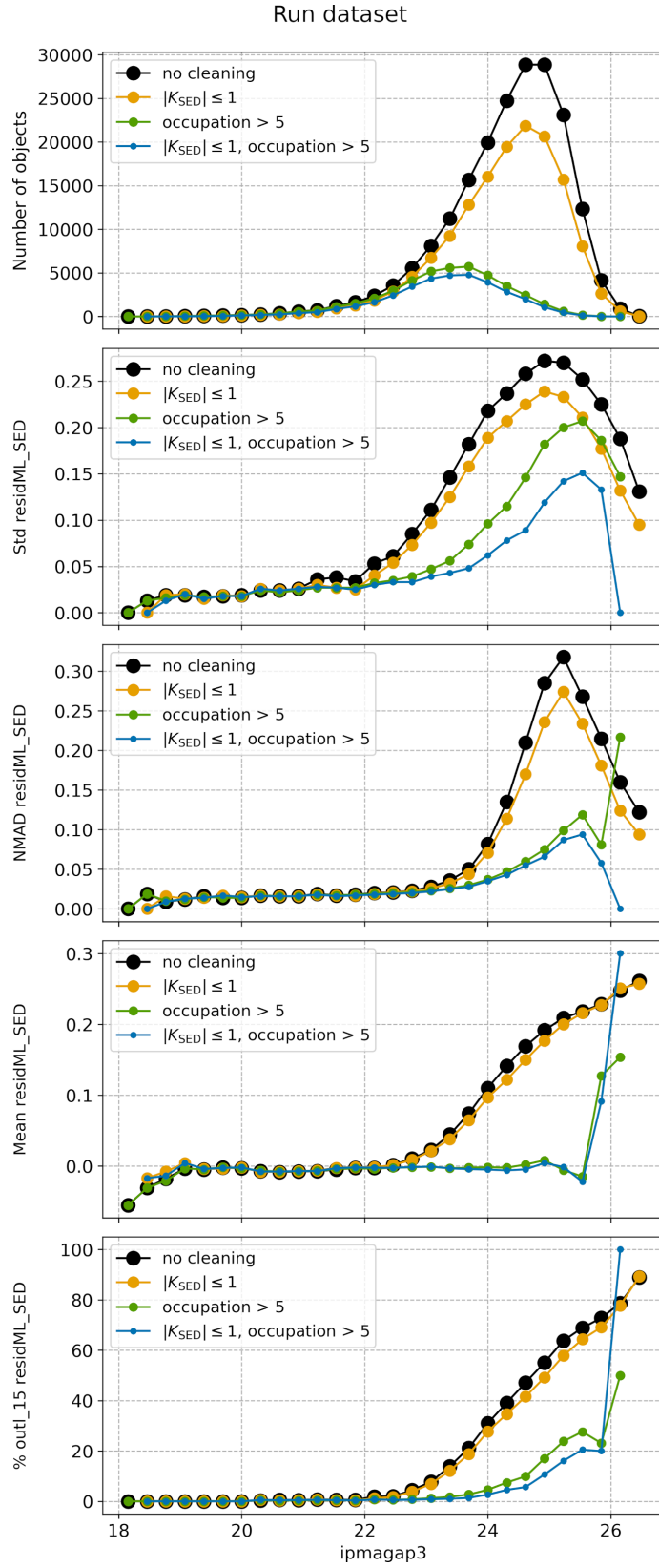


Figure 9. Statistics for ML/SED residuals for run dataset in *ipmagap3* bins after applying different filters. Bins with number of objects < 15 are considered to be unreliable and excluded from these plots.

- Masters D. C., Stern D. K., Cohen J. G., Capak P. L., Rhodes J. D., Castander F. J., Paltani S., 2017, *ApJ*, 841, 111
- McCracken H. J., et al., 2012, *A&A*, 544, A156
- Newman J. A., 2008, *ApJ*, 684, 88
- Nicastro F., et al., 2018, *Nature*, 558, 406
- Nocedal 2006, Numerical optimization / Jorge Nocedal, Stephen J. Wright, 2nd edition edn. Springer Series in Operations Research and Financial Engineering, Springer, Berlin
- Norris R. P., et al., 2019, *PASP*, 131, 108004
- Pasquet J., Bertin E., Treyer M., Arnouts S., Fouchez D., 2019, *A&A*, 621, A26
- Polsterer K. L., Gieseke F., Igel C., Goto T., 2014, in Manset N., Forshay P., eds, Astronomical Society of the Pacific Conference Series Vol. 485, Astronomical Data Analysis Software and Systems XXIII. p. 425
- Rhodes J., et al., 2017, *ApJS*, 233, 21
- Rosenblatt F., 1963, *American Journal of Psychology*, 76, 705
- Sadeh I., Abdalla F. B., Lahav O., 2016, *PASP*, 128, 104502
- Salvato M., Ilbert O., Hoyle B., 2019, *Nature Astronomy*, 3, 212
- Schmidt S. J., et al., 2020, *MNRAS*, 499, 1587
- Scoville N., et al., 2007, *ApJS*, 172, 1
- Vettigli G., 2018, MiniSom: minimalistic and NumPy-based implementation of the Self Organizing Map, <https://github.com/JustGlowing/minisom/>
- Way M. J., Klose C. D., 2012, *PASP*, 124, 274
- Wright A. H., et al., 2019, *A&A*, 632, A34

APPENDIX A: ADDITIONAL INFORMATION ON DATA PROCESSING AND ITS EFFECTS ON THE REDSHIFT DISTRIBUTIONS

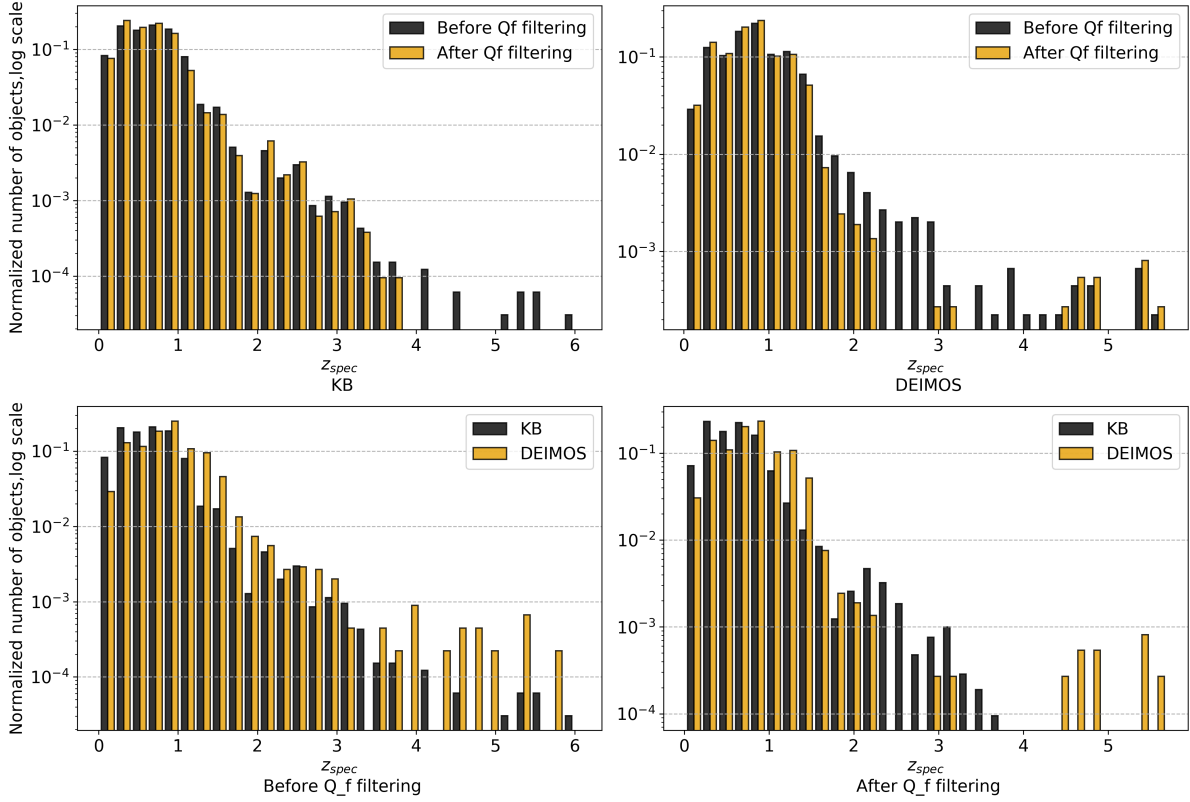


Figure A. 1. Normalized spec-z distribution before and after quality flag (Q_f) cleaning of the KB and DEIMOS datasets. The plots in the top row compare distributions dataset-wise, while the plots in the bottom row compare the KB and DEIMOS on the same cleaning stages.

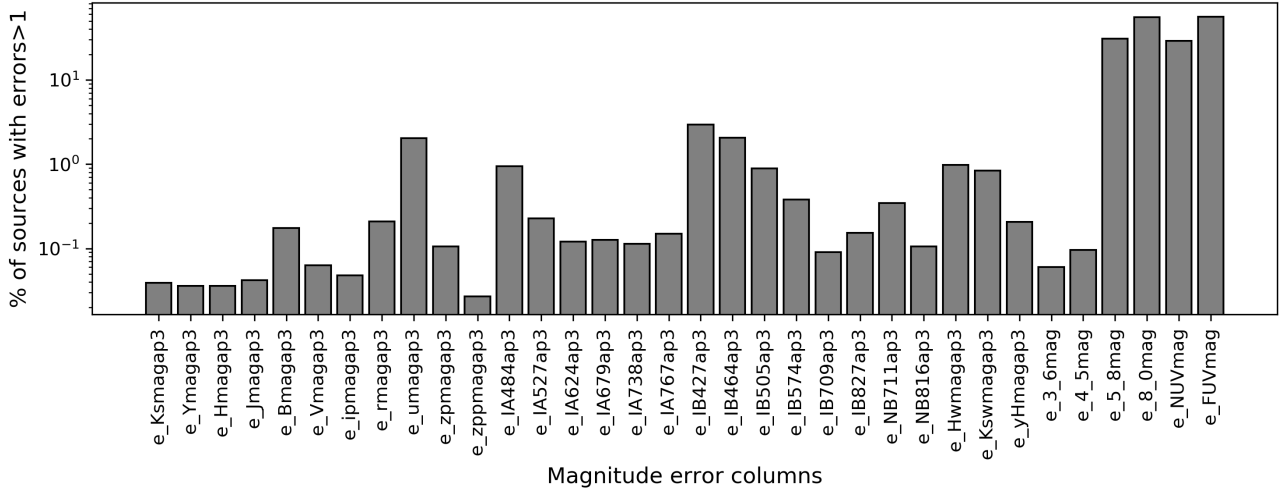


Figure A. 2. Number of objects in the KB with magnitude errors > 1 by bands.

This paper has been typeset from a $\text{\TeX}/\text{\LaTeX}$ file prepared by the author.

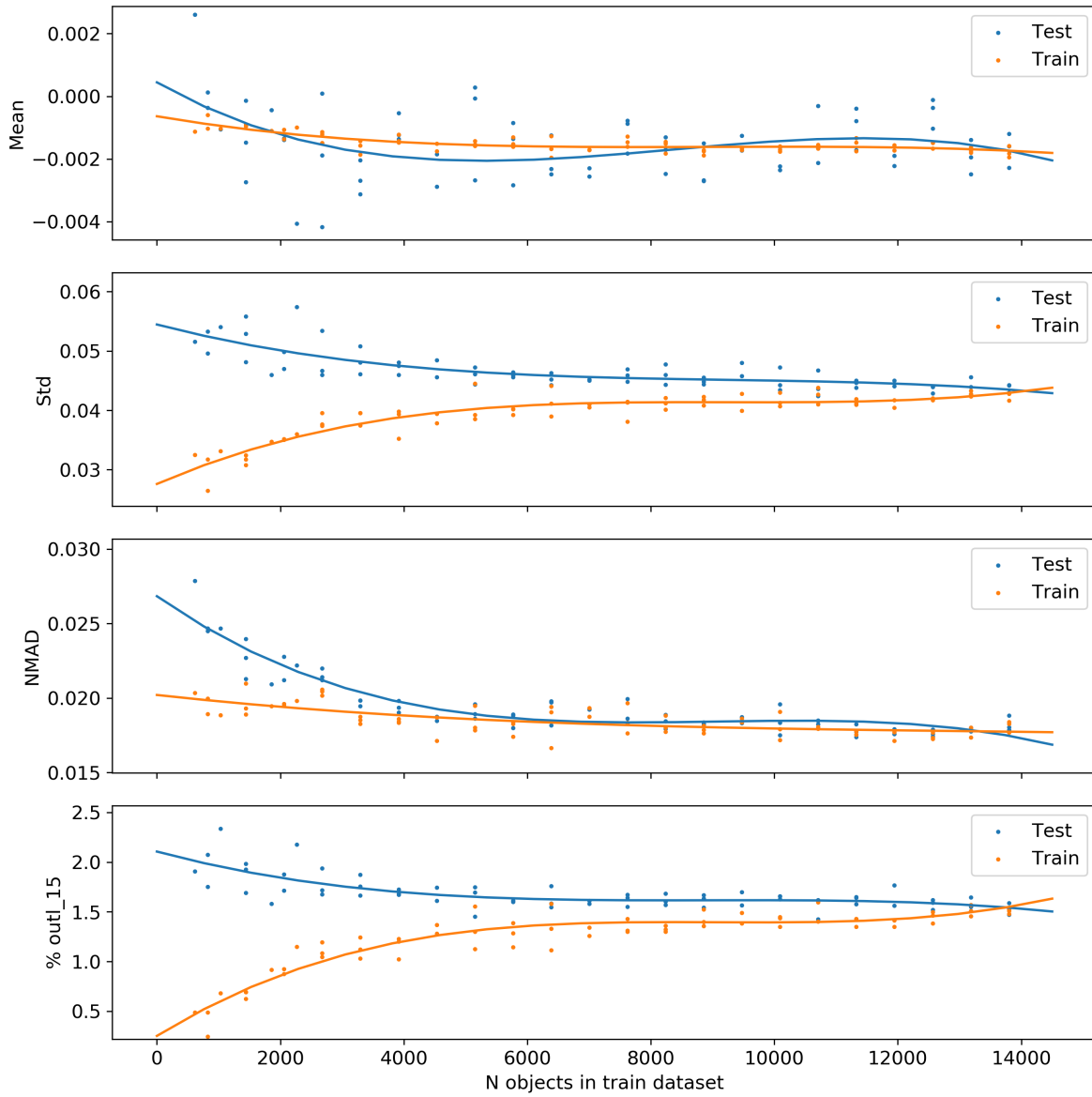


Figure A. 3. The change of quality of photo-z predictions with the increase of the size of the training sample. Using NMAD as the most stable metric we can see that the training sample as small as ~ 6000 objects provides enough generalization for the model.

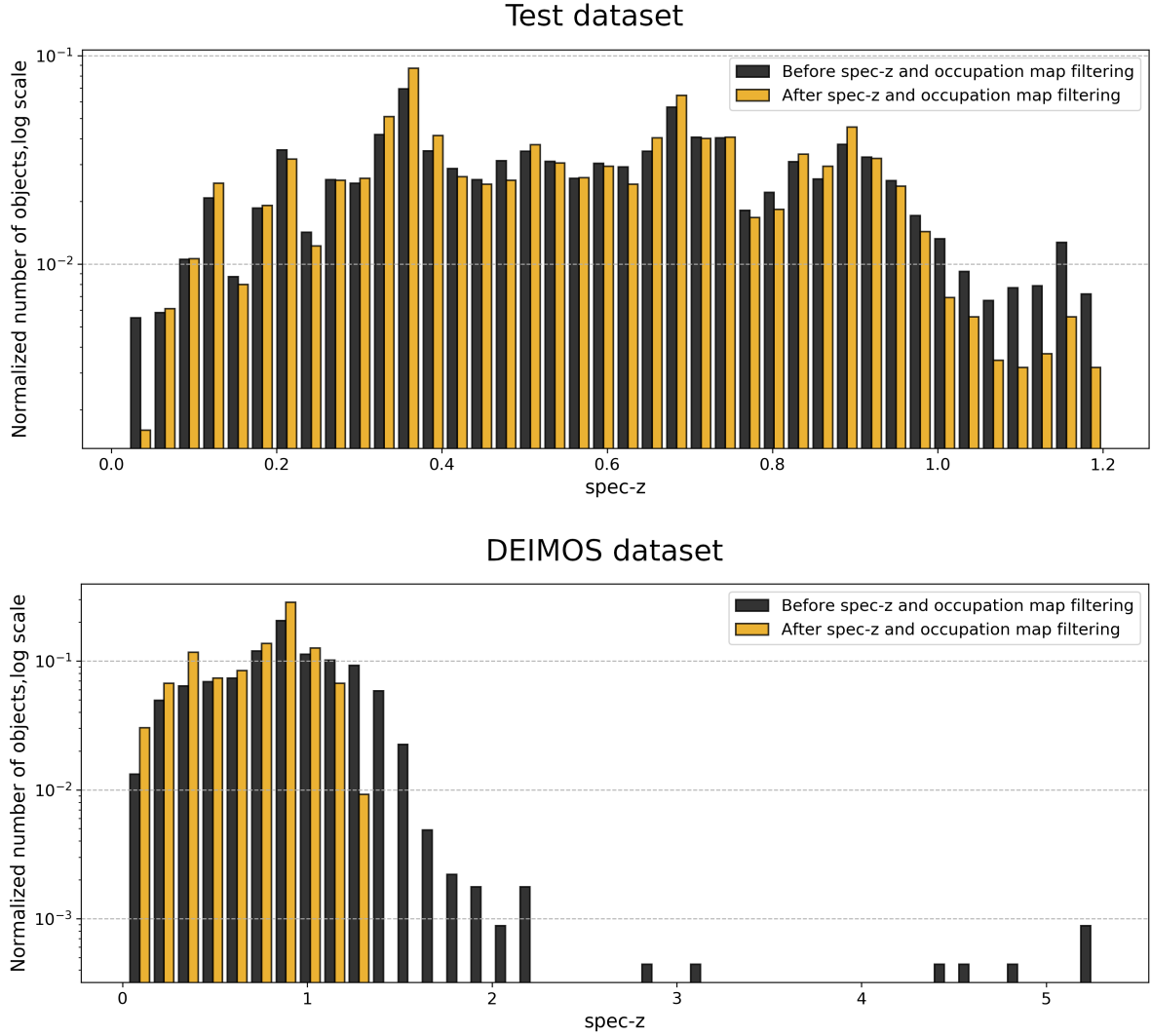


Figure A. 4. Spec- z distributions before and after SOM cleaning (using both K_{spec} filtering and occupation maps cleaning). The normalized distribution of spec- z of the test sample (upper panel) does not change much. After the cleaning, there is a diminishing of the number of objects with $z_{spec} < 0.02$ and much softer decline of the relative share of objects with $1 < z_{spec} < 1.2$, but the shape of the middle part of the distribution remains intact. The lower panel shows that in the case of the DEIMOS, the SOM cleaning procedures do exactly what they are supposed to do: remove objects with z_{spec} higher than 1.2, which was the limit for the KB.

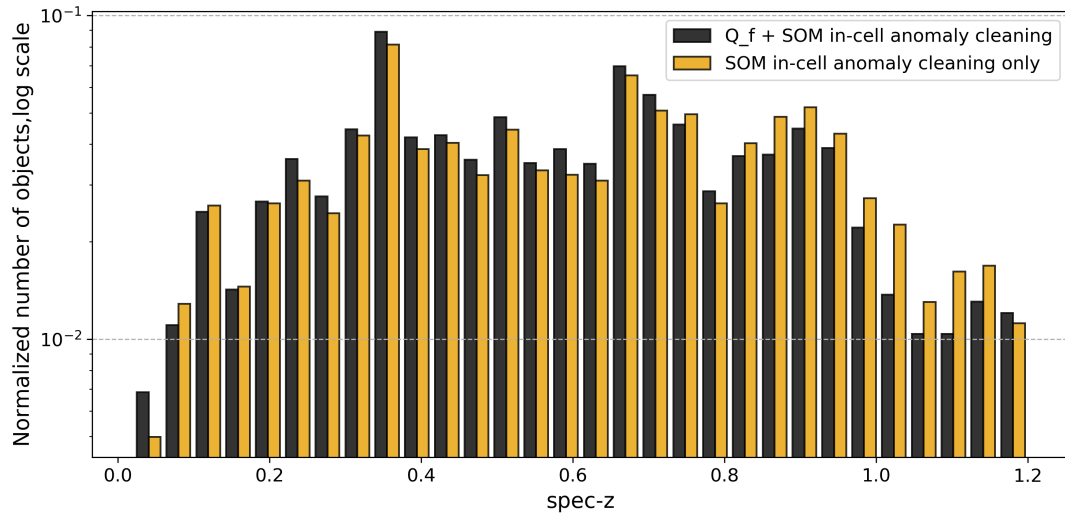


Figure A. 5. Spec- z distribution for the test dataset with and without standard Q_f cleaning. The shapes of both distributions are very close, although SOM-only cleaning preserves slightly more high-redshift objects.